



Kaunas University of Technology
Faculty of Mathematics and Natural Sciences

Influence of medical implant materials on the appearance of medical imaging artifacts

Master's Final Degree Project

Mantas Brukštus

Project author

Assoc. prof. Benas Gabrielis Urbonavičius

Supervisor

Kaunas, 2022



Kaunas University of Technology
Faculty of Mathematics and Natural Sciences

Influence of medical implant materials on the appearance of medical imaging artifacts

Master's Final Degree Project
Medical Physics (6213GX001)

Mantas Brukštus

Project author

**Assoc. prof. Benas Gabrielis
Urbonavičius**

Supervisor

Prof. Liutauras Marcinauskas

Reviewer

Kaunas, 2022



Kaunas University of Technology
Faculty of Mathematics and Natural Sciences
Mantas Brukštus

Influence of medical implant materials on the appearance of medical imaging artifacts

Declaration of Academic Integrity

I confirm the following:

1. I have prepared the final degree project independently and honestly without any violations of the copyrights or other rights of others, following the provisions of the Law on Copyrights and Related Rights of the Republic of Lithuania, the Regulations on the Management and Transfer of Intellectual Property of Kaunas University of Technology (hereinafter – University) and the ethical requirements stipulated by the Code of Academic Ethics of the University;
2. All the data and research results provided in the final degree project are correct and obtained legally; none of the parts of this project are plagiarised from any printed or electronic sources; all the quotations and references provided in the text of the final degree project are indicated in the list of references;
3. I have not paid anyone any monetary funds for the final degree project or the parts thereof unless required by the law;
4. I understand that in the case of any discovery of the fact of dishonesty or violation of any rights of others, the academic penalties will be imposed on me under the procedure applied at the University; I will be expelled from the University and my final degree project can be submitted to the Office of the Ombudsperson for Academic Ethics and Procedures in the examination of a possible violation of academic ethics.

Mantas Brukštus

Confirmed electronically

Mantas Brukštus. Influence of medical implant materials on the appearance of medical imaging artifacts. B000M004 Final project / supervisor Assoc. prof. Benas Gabrielis Urbonavičius; Faculty of Mathematics and Natural Sciences, Kaunas University of Technology.
Study field and area (study field group): Medical Technologies, Health sciences.
Keywords: MRI, CT, US, Artifacts, Artifact reduction, GAN, MIC.
Kaunas, 2022. 49 pages.

Summary

Magnetic resonance imaging (MRI), computed tomography (CT) and ultrasonography/ultrasound (US) are sophisticated diagnostic modalities that are utilized in medical imaging in diagnostic field. Unfortunately, all materials react differently and uniquely to the physics behind the MRI, CT and US modalities. As a result, negative effect such as artifact creation occur, which leads to uninterpretable medical images in specific areas of interest. In order to know how big of an area will be covered up by artifact induced medical implants, 3D Slicer and Image J applications will be used with thresholding, contouring technique and contrast to noise ratio calculation to be able to assess the artifact affected volume, area and effect on the image interpretability. This method was used on five samples, stainless steel, aluminium metal, dental implant material of Zr series Katana Zirconia STML. Dental filling of K series ENAMEL plus HRi biofunction (MICERIUM S.p.A, Italy). Dental implant material of E-max series Ivoclar Vivadent IPS E.max press, which are the most popular materials for head and neck region medical implants, while scanning with three different medical imaging modalities (MRI, CT and US). The results have shown that the biggest artifact volume was observed in CBCT kV imaging with water, with values ranging from 3344.54 mm³ to 16720.87 mm³, and the smallest artifact volume was detected in CBCT MV imaging without water, with ranges from 301.115 mm³ to 1074.75 mm³. Stainless steel sample has proved to be the most artifacting medical material, with volume values ranging from 1074.75 mm³ to 25493.33 mm³ across modalities, whereas K sample has shown the least amount of artifacting, with values from 266.79 mm³ to 6855.21 mm³ across imaging modalities.

Mantas Brukštus. Medicininių implantų medžiagų įtaka medicininių vaizdų artefaktų atsiradimui. Magistro baigiamasis projektas / doc. dr. Benas Gabrielis Urbonavičius; Kauno technologijos universitetas, Matematikos ir gamtos mokslų fakultetas.

Studijų kryptis ir sritis (studijų krypčių grupė): Medicinos technologijos, Sveikatos mokslai.

Reikšminiai žodžiai: MRT, KT, Ultrasonografija, Artefaktai, Artefaktų šalinimas, GAN, MIC.

Kaunas, 2022. 49 puslapiai.

Santrauka

Magnetinio rezonanso tomografija (MRT), kompiuterinė tomografija (KT) ir ultragarsas (US) - tai sudėtingi diagnostikos būdai, kurie naudojami medicininio vaizdavimo diagnostikos srityje. Visos medžiagos skirtingai ir unikalios reaguoja į magnetinio rezonanso tomografiją, kompiuterinę tomografiją ir ultragarsą, dėl šių įrenginių veikimo principų. Dėl to atsiranda neigiamas poveikis, pavyzdžiui, artefaktų susidarymas, todėl tam tikrose dominančiose srityse medicininiai vaizdai tampa neinterpretuojami. Norint sužinoti, kokio dydžio plotas bei tūris bus padengtas artefakto sukeltais medicininiais implantais, bus naudojamos 3D Slicer ir Image J programos su slenksčio (angl. *thresholding*) nustatymo, kontūravimo technika ir kontrasto ir triukšmo santykio apskaičiavimu, kad būtų galima įvertinti artefakto paveiktą tūrį, plotą ir poveikį vaizdo interpretacijai. Šis metodas taikytas penkiems bandiniams, nerūdijančiam plienui, aliuminiui, Zr serijos dantų implantų medžiagai Katana Zirconia STML. Dantų plombos iš K serijos ENAMEL plus HRi biofunkcijos (MICERIUM S.p.A, Italija). E-max serijos dantų implantų medžiaga Ivoclar Vivadent IPS E.max press, kurios yra populiariausos galvos ir kaklo srities medicininių implantų medžiagos, skenuojant trimis skirtingais medicininio vaizdavimo būdais (MRT, KT ir US). Rezultatai parodė, kad didžiausias artefakto tūris nustatytas CBCT kV vaizdavimo su vandeniu metu - nuo 3344,54 mm³ iki 16720,87 mm³, o mažiausias artefakto tūris nustatytas CBCT MV vaizdavimo be vandens metu - nuo 301,115 mm³ iki 1074,75 mm³. Nerūdijančio plieno mėginys pasirodė esąs daugiausiai artefaktų sukelianti medicininė medžiaga, kurios tūrio vertės įvairiuose vaizdavimo būduose svyravo nuo 1074,75 mm³ iki 25493,33 mm³, o K mėginys pasižymėjo mažiausiu artefaktų kiekiu, kurio vertės įvairiuose vaizdavimo būduose svyravo nuo 266,79 mm³ iki 6855,21 mm³.

Table of contents

List of figures	7
List of tables	8
Introduction	9
1. Literature review	10
1.1. Magnetic resonance imaging	10
1.2. Computed tomography	10
1.3. Ultrasonography (Ultrasound).....	11
1.4. Imaging artifact	11
1.5. Magnetic susceptibility and permeability.....	18
1.6. Artifact reduction methods in MRI	20
1.7. Artifact reduction methods in CT.....	21
1.8. Artifact reduction methods in US.....	23
1.9. Medical implant materials	24
1.9.1. Stainless steel.....	25
1.9.2. Aluminium.....	27
1.9.3. E-max	27
1.9.4. Zirconia.....	28
1.9.5. K.....	28
2. Materials and methods	29
3. Results	31
3.1. CBCT and MRI artifacting results	33
3.2. US artifacting results	34
3.3. CNR calculation results	38
Conclusions	41
List of references	42

List of figures

Figure 1. Head CT with dental fillings before (a) and after (b) the use of MAR [53]	22
Figure 2. Schaeffler diagram for stainless steels [78].....	26
Figure 3. US 6.5 MHz rounded probe (a) and 7.5 MHz linear probe (b) [97, 98]	29
Figure 4. 3D modelled sample holder	30
Figure 5. Upper image: Ivoclar Vivadent IPS E.max press (E-max), Katana Zirconia STML (Zr) and ENAMEL plus HRi biofunction (K) samples; Image on the left: E-max sample atomic force microscopy image [99]; Image on the right: Zr sample atomic force microscopy image [100].	30
Figure 6. Prepared samples for imaging without adding water	31
Figure 7. Measuring the affected artifact area with Image J by contouring the artifact and subtracting the implant material.	31
Figure 8. Workflow of artifacting volume determination of CBCT kV without water Zr sample while applying thresholding in 3D Slicer application	32
Figure 9. US imaging of Zr sample in water with 7.5 MHz probe	35
Figure 10. US imaging of Zr sample in water with 6.5 MHz probe	35
Figure 11. US imaging of Stainless steel (SS) sample in water with 7.5 MHz probe.....	35
Figure 12. US imaging of Stainless steel (SS) sample in water with 6.5 MHz probe.....	35
Figure 13. US imaging of K sample in water with 7.5 MHz probe	36
Figure 14. US imaging of K sample in water with 6.5 MHz probe	36
Figure 15. US imaging of E-max sample in water with 7.5 MHz probe	36
Figure 16. US imaging of E-max sample in water with 6.5 MHz probe	36
Figure 17. US imaging of Aluminium (Al) sample in water with 7.5 MHz probe	36
Figure 18. US imaging of Aluminium (Al) sample in water with 6.5 MHz probe	36
Figure 19. Overlay of all artifacts in a single slice Zr sample. CBCT kV with water (Green), CBCT kV without water (Blue), CBCT MV with water (Yellow), CBCT MV without water (Teal), MRI (Red).	37
Figure 20. Overlay of all artifacts in a single slice SS sample. CBCT kV with water (Green), CBCT kV without water (Blue), CBCT MV with water (Yellow), CBCT MV without water (Teal), MRI (Red).	37
Figure 21. Overlay of all artifacts in a single slice K sample. CBCT kV with water (Green), CBCT kV without water (Blue), CBCT MV with water (Yellow), CBCT MV without water (Teal), MRI (Red).	37
Figure 22. Overlay of all artifacts in a single slice E-max sample. CBCT kV with water (Green), CBCT kV without water (Blue), CBCT MV with water (Yellow), CBCT MV without water (Teal), MRI (Red).	37
Figure 23. Overlay of all artifacts in a single slice Al sample. CBCT kV with water (Green), CBCT kV without water (Blue), CBCT MV with water (Yellow), CBCT MV without water (Teal), MRI (Red).	37

List of tables

Table 1. Most common artifacts, which are observed due to imaged material sound absorption or reflection in US modality [17, 18, 19, 23].....	12
Table 2. Most common artifacts, which are observed due to sound wave being stuck in US modality [14, 16, 21, 22]	13
Table 3. Most common artifacts, which are dependent on the angle of the probe in US modality [14, 15, 20].....	14
Table 4. Most common artifacts in CT modality [24, 25, 26, 34]	15
Table 5. Most common artifacts in MRI modality, which relate to magnetic effect and tissue imaging angle [31, 32, 35, 35, 40].....	16
Table 6. Most common artifacts in MRI modality, which relate to electronic noise or signal reception [28, 29, 30].....	17
Table 7. Most common artifacts, which occur due to K-space errors and uneven excitation in MRI modality [27, 33]	18
Table 8. Material classification based on interactions with magnetic field [40]	19
Table 9. Listing of orthodontic appliance compatibility with magnetic field [14] $\Delta\chi$ – susceptibility difference between susceptibility of material and susceptibility of water. SE – Spin Echo, GRE – Gradient Echo. [37]	20
Table 10. Comparison of artifact reduction methods in MRI, CT and US systems [3, 6, 8, 43, 44, 56, 57, 60, 61, 63, 64].....	24
Table 11. Differences between Austenitic stainless steels and Martensitic stainless steels [76, 77] 26	
Table 12. Comparison of mechanical, physical and chemical properties of K and Emax samples [81, 82, 87, 88]	28
Table 13. Artifact affected volume in CBCT kV and MV with water and without	33
Table 14. Artifact affected volume in MRI with Sag T1 TSE sequence with water	33
Table 15. View of the biggest artifacting area of each imaged sample in CBCT and MRI modalities	34
Table 16. Artifact affected area in US with 7.5 MHz and 6.5 Mhz probes	35
Table 17. CNR results after measuring and comparing unaffected and affected images in MRI ...	38
Table 18. CNR results after measuring and comparing unaffected and affected images in CBCT kV with water	38
Table 19. CNR results after measuring and comparing unaffected and affected images in CBCT kV without water.....	39
Table 20. CNR results after measuring and comparing unaffected and affected images in CBCT MV with water.....	39
Table 21. CNR results after measuring and comparing unaffected and affected images in CBCT MV without water.....	40

Introduction

Medical implants are devices composed of synthetic materials which are implanted into the human body for medical reasons, typically for a long time. They could be used to substitute body components like hips and knees, distribute medicine like pain relievers, monitor and control bodily processes like heart rate, and support organs and tissues [1]. Surgical meshes and stents are examples of inert implants that are used to give structural support. Others are more active, interacting with the body. [1, 2] These implanted medical materials' features and characteristics have been thoroughly researched and characterised. However, their overall impact on image quality in magnetic resonance imaging, computed tomography and ultrasound imaging is not thoroughly explored as there is a lack of research papers on this subject. Orthodontic implants are the most widely utilised, artifacts induced by dental materials can significantly reduce MRI and CT image quality, limiting their diagnostic use [2, 3]. Artifacts can conceal a pathology or the anatomy of the region being evaluated, making it harder to find anatomical structures for surgical treatments. Streak artifacts are a prevalent issue in CT imaging. This form of artifacts can be caused by the presence of high attenuation metal objects in the field of view, such as orthodontic bands, dental restorations, surgical plates, and screws [3]. This is due to the fact that metal materials strongly attenuate the X-ray beam, resulting in incorrectly high attenuation values for items behind the metal. MRI, on the other hand, utilizes a mixture of a strong uniform magnetic field and radio frequency pulses to make images [5]. When put in a magnetic field, all substances get magnetised to varying degrees, based on their magnetic susceptibility values and in the images, these artifacts appear as geometric distortions as well as dark holes or bright patches of signal pile-up [4, 5]. Whereas artifacts in ultrasonography (US) can lead to structures appearing in an image that are not anatomically there, or structures that should be anatomically present to be missing from the image [6]. Structures in US artefacts may also be present but inaccurate in position, brightness or size. The US is prone to a variety of imaging artifacts, which are frequently observed in medical practice. Artifacts have the tendency to obstruct image perception and interpretation [6, 7].

Main aim:

To evaluate the scale of image artifacts caused by implant materials in different medical imaging modalities.

Tasks:

1. Analyse the causes of artifacts in medical images and their reduction methods
2. Determine the most common materials for the head and neck region
3. Develop a measurement method for artifacting evaluation
4. Perform artifacting evaluation with select materials in US, MRI and CT.

1. Literature review

1.1. Magnetic resonance imaging

MRI is a complex imaging modality, which working principle can be divided into four categories: preparation, excitation, spatial encoding and signal acquisition [8].

Preparation begins when the patient is positioned in a static magnetic field created by the MRI scanner's magnet. Countless hydrogen atoms are found in biological tissues, either in water molecules or in a variety of other compounds. The proton, which is the nucleus of hydrogen, has an inherent magnetism known as spin [8]. The Larmor frequency, which is proportional to the magnetic field strength, rotates the spin magnetisation vector around the magnetic field. All protons within the tissues align parallel to the magnetic field as a result of this magnetisation. The parallel magnetisation scales with the magnetic field intensity; at 3 T, it will be around double that of 1.5 T [9].

In the excitation phase, the scanner emits a radiofrequency (RF) pulse during the image acquisition procedure. The RF pulse is in resonance when tuned to the Larmor frequency: it causes phase coherence in the precession of all proton spins. The RF pulse's length is designed so that the spin magnetisation is tilted perpendicular to the magnetic field. The nuclear magnetic resonance (NMR) signal is generated when a receiving coil is placed near the tissue and the transverse magnetisation, which is still rotating as the Larmor precession, generates an electric current in the coil via Faraday induction [9]. Two simultaneous relaxation processes diminish the NMR signal. The NMR signal is attenuated by a time constant termed the transverse relaxation period when the spin system loses coherence, thus T2 sequence is made. During this period, the magnetisation vector steadily relaxes towards its equilibrium orientation, which is parallel to the magnetic field: this is known as the spin-lattice relaxation time, which creates the T1 sequence. The difference in T1 and T2 relaxation periods between various tissues causes different contrast in MRI [8, 9].

Magnetic field gradients (smaller extra magnetic fields whose intensity is linearly proportional to their spatial position) are used to encode the MRI signal's spatial information: protons spin at slightly different speeds in various regions. Lorentz force is then exerted on the coils by the portion of the gradient coils and associated current that is perpendicular to the main magnetic field [9]. During the MR image acquisition process, the gradients are switched on and off very fast, forcing them to vibrate intensely and creating the majority of the acoustic noise [8, 9].

The NMR signal acquired using magnetic field gradients has distinct frequencies corresponding to different tissue spin orientations and is referred to as the MRI signal. The analogue MRI signal is digitised and stored after sampling for processing, which involves separating the signal contributions from different spatial regions indicated via pixels inside the processed image. Fourier transform is used to achieve all of this [8, 9].

1.2. Computed tomography

Computed tomography (CT) is a type of imaging that employs X-rays to create cross-sectional images of the body. Cross-sections are then created by measuring the attenuation coefficients of X-ray beams as they travel through the volume of the material being researched. CT is founded on the fundamental idea that the attenuation coefficient may be used to calculate the density of the tissue traversed by the X-ray beam [10,11]. Using this technique, CT allows for the reconstruction of body density via a two-dimensional section perpendicular to the acquisition system's axis. The CT X-ray tube generates N photons per unit of time (usually at energy levels between 20 and 150 keV).

Generated X-rays produce a beam that passes through a biological material layer with a thickness of x . A detector at the sample's exit counts $N + \Delta N$ photons, with N being less than 0. The X-ray beam's attenuation values are registered, and the information is utilised to create a 3D model of the scanned object/tissue [11]. The CT scanner's detectors, unlike those used in x-ray radiography, do not create an image. They test the transmission of a narrow X-ray beam across a whole body CT scan. Image of that portion is acquired out of several angles, allowing the depth information to be retrieved (in the 3-D). The computer utilises complicated mathematical procedures to recreate tomographic pictures of the patient from the "precompiled" CT information [10, 11].

1.3. Ultrasonography (Ultrasound)

Ultrasound is a technique for diagnosing and treating patients that uses high-frequency sound. The range of ultrasound frequencies is 2 to 15 MHz. Mechanical oscillations of many crystals in a transducer, which are stimulated by electrical pulses, produce the ultrasonic beam by piezoelectric effect [13]. The transducer is a device that transforms one type of energy into another. The ultrasonic waves (sound pulses) are emitted from the transducer, move through various tissues, and then rebound back as reflected echoes to the transducer. The transducer crystals transform the returned echoes back into electrical impulses, which are then processed to generate the ultrasound image displayed on the screen. Ultrasound transducers have a bandwidth, or range of ultrasound frequencies, where general abdominal imaging, uses 2.5-3.5 MHz and superficial imaging, uses 5.0-7.5 MHz [12, 13].

Ultrasound waves are reflected at the surfaces of tissues with various densities, with the reflection corresponding to the impedance difference. The proportion of reflected sound increases as the density difference grows, whereas the proportion of transmitted sound decreases proportionally. When the tissue density difference is large, the sound is entirely reflected, resulting in total acoustic shadowing [12].

1.4. Imaging artifact

The term "artifact" in radiology refers to something that appears on an image but in reality it is non-existent due to a quirk of the imaging modality itself. Clothing, medical implants, body parts, and other factors outside the patient might obscure or distort the image, which is referred to as an artifact. Image noise is usually the most frequent artefact encountered in radiography, and it is present in every modality and method. It can be reduced but never completely removed. Most common artifacts for each modality are shown in tables from 1 to 7, but the list is not conclusive as there are rare artifacts, which appear on extremely specific circumstances.

Table 1. Most common artifacts, which are observed due to imaged material sound absorption or reflection in US modality [17, 18, 19, 23]




Modality	Example image	Artifact
US		<p><i>Acoustic enhancement</i></p> <p>Appears due to amplified echoes in deep structures that transmit sound effectively (ex. cyst) [23]</p>
US		<p><i>Acoustic shadowing</i></p> <p>Materials, which extremely absorb or reflect sound waves produce acoustic shadowing (ex. bone, implants) [19]</p>
US		<p><i>Comet tail artifact</i></p> <p>Imaging of tiny extremely reflective objects produces the comet tail artifact [17, 18]</p>

Table 2. Most common artifacts, which are observed due to sound wave being stuck in US modality [14, 16, 21, 22]

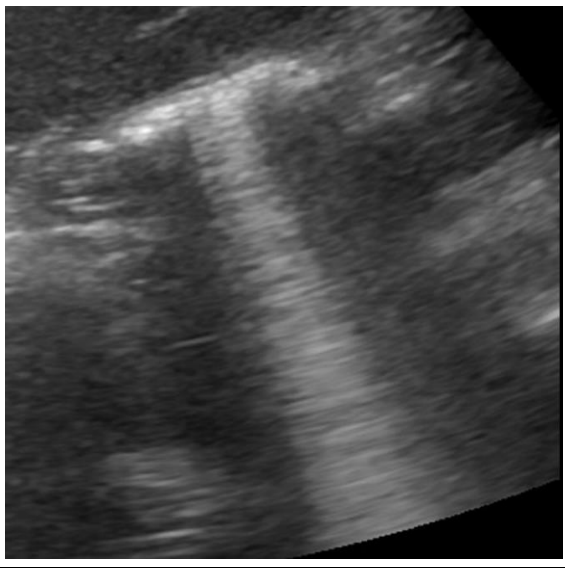

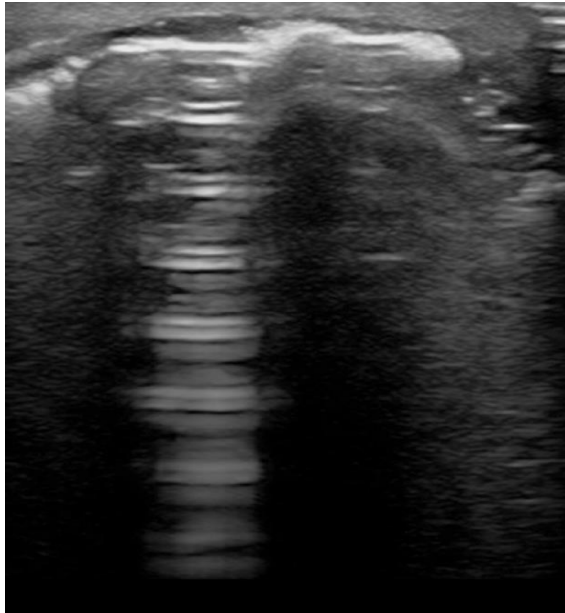
US		<p><i>Ring down artifact</i></p> <p>Occurs if sound wave hits 4 air bubbles in specific formation (inverted tetrahedron), gets trapped and continuously resonates [16]</p>
US		<p><i>Mirror image artifact</i></p> <p>Reflected beam on the way back to transducer encounters extremely reflective surface and bounces twice from the same initial location before finally reaching the transducer [21, 22]</p>
US		<p><i>Reverberation artifact</i></p> <p>Occurs when beam gets stuck between two reflective surfaces and transducer detects it later than supposed, therefore the depth position of the object is misread [14]</p>

Table 3. Most common artifacts, which are dependent on the angle of the probe in US modality [14, 15, 20]

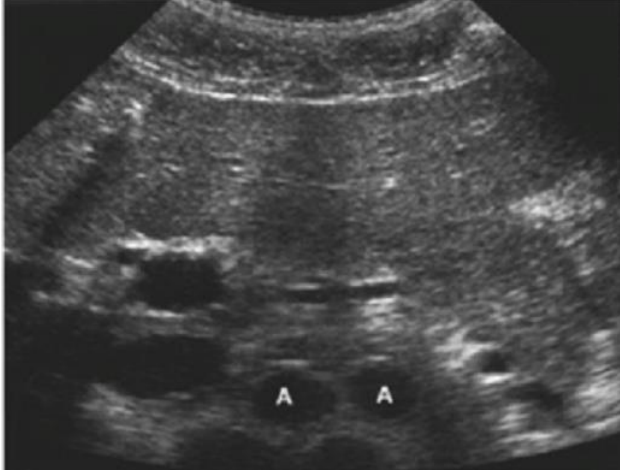
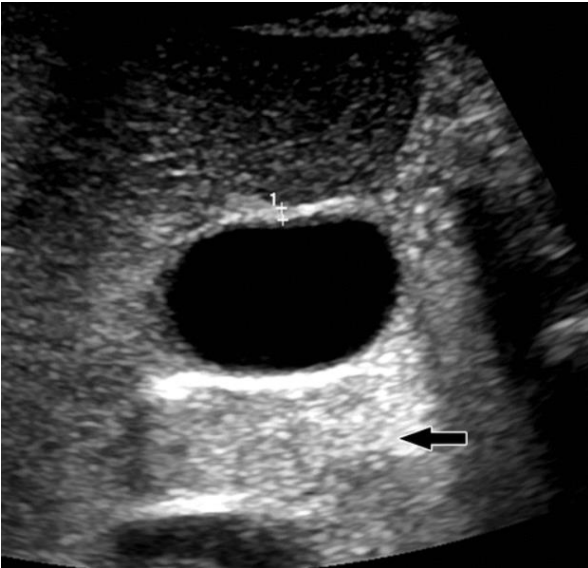
US		<p><i>Refraction artifact</i></p> <p>If ultrasound pulse hits the object non-perpendicularly, refraction artifact occurs, which is mitigated by increased difference on propagation speeds between tissues [14]</p>
US		<p><i>Speckle artifact</i></p> <p>Scattering of waves from the surface produces the speckle artifact, which looks like a texture [15, 20]</p>

Table 4. Most common artifacts in CT modality [24, 25, 26, 34]

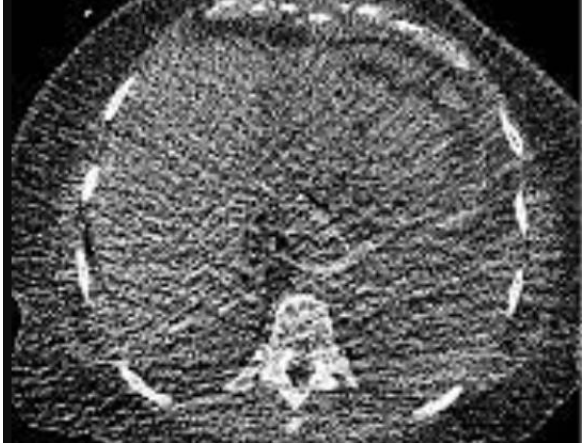

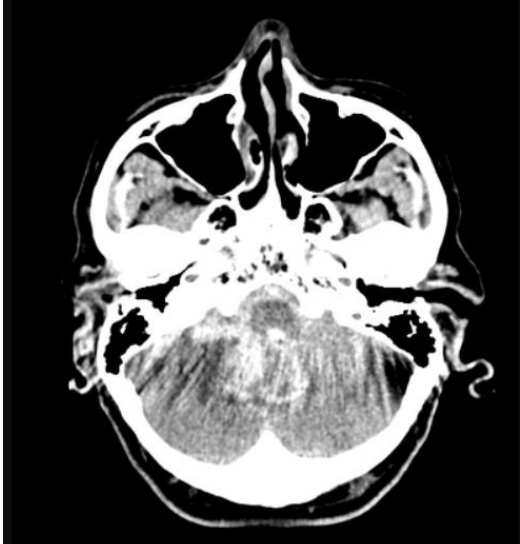
CT		<p><i>Quantum mottle</i> Occurs when number of photons that reach the detector fluctuates immensely [25, 34]</p>
CT		<p><i>Photon starvation</i> If imaged object has high attenuation (metal object), not enough photons reach the detector and photon starvation is observed [24, 26]</p>
CT		<p><i>Beam hardening</i> If low energy photons get selectively attenuated, then only high energy photons make the beam and beam hardening artifact appears [24]</p>

Table 5. Most common artifacts in MRI modality, which relate to magnetic effect and tissue imaging angle [31, 32, 35, 35, 40]

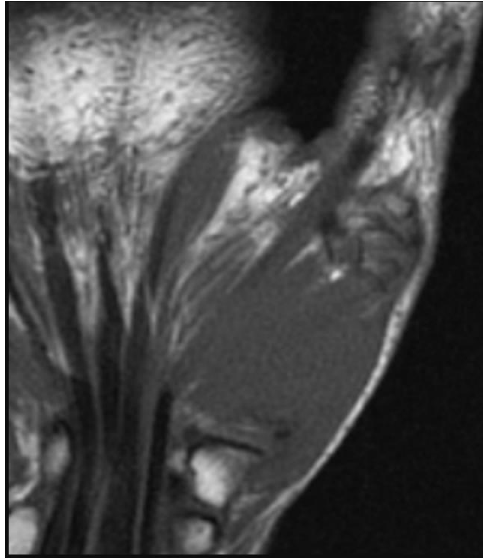
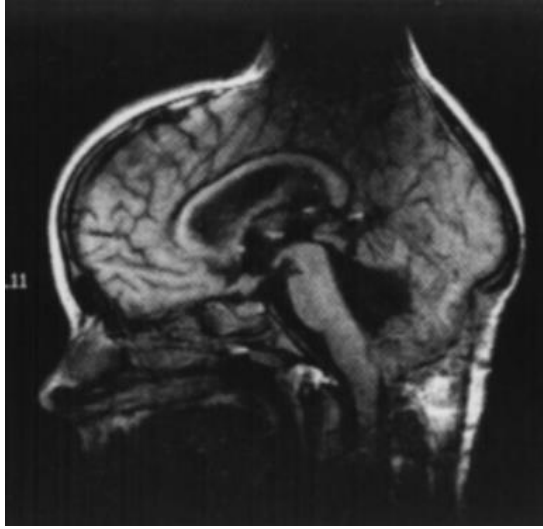
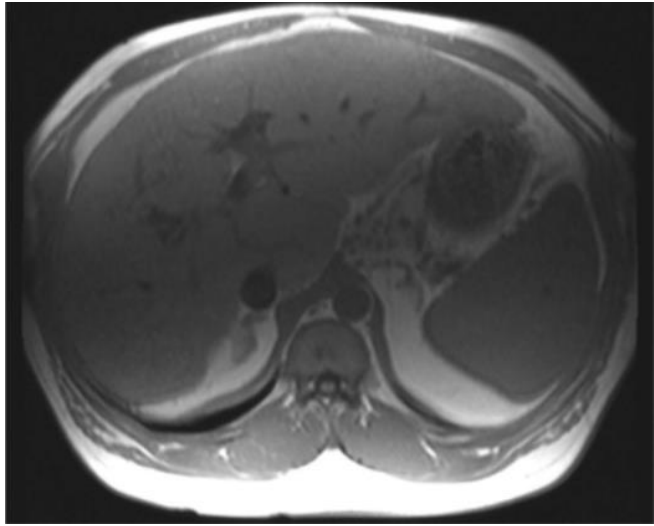
MRI		<p><i>Magic angle effect</i></p> <p>Appears in T1 weighted (short TE) sequences. Confined to region of tightly bound collagen, which is at 54.74° from the main magnetic field [32]</p>
MRI		<p><i>Magnetic susceptibility artifact</i></p> <p>Occurs when any type of object in ferromagnetic and/or paramagnetic categories distort the signal [39, 40]</p>
MRI		<p><i>Chemical shift artifact</i></p> <p>Occurs when fat molecules and water molecules are spatially misregistered during frequency encoding direction [31, 35]</p>

Table 6. Most common artifacts in MRI modality, which relate to electronic noise or signal reception [28, 29, 30]



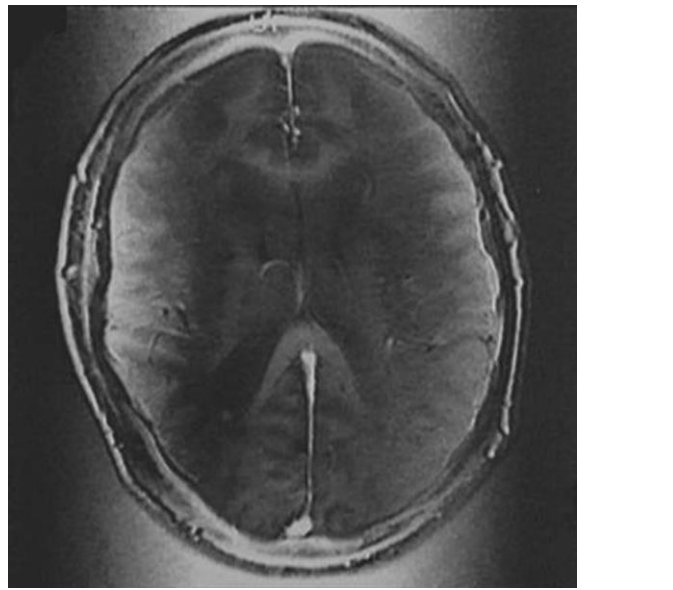
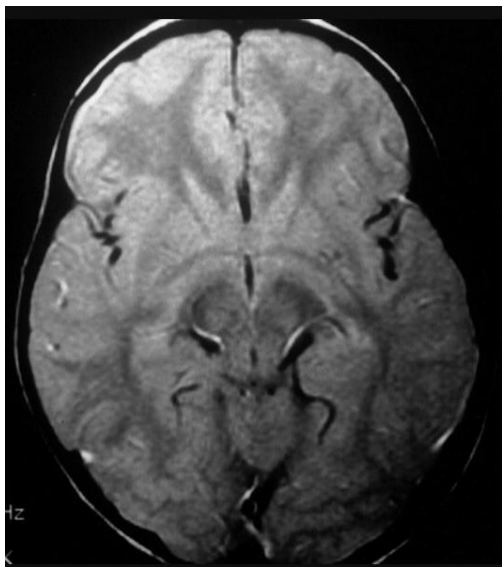

MRI		<p><i>Dielectric effect</i></p> <p>If patients scanning location size exceeds the radiofrequency wavelength (RF wavelength in air 234 cm; At 3T, RF wavelength in human is 23 cm), the dielectric effect appears [30]</p>
MRI		<p><i>Zipper artifact</i></p> <p>Electronic noise interference causes the zipper artifact to appear and no solution for it exists [29]</p>
MRI		<p><i>Radiofrequency overflow artifact</i></p> <p>Occurs when signal received from the patient is too intense due to malfunctioned receiver [28]</p>

Table 7. Most common artifacts, which occur due to K-space errors and uneven excitation in MRI modality [27, 33]

MRI		<p><i>Shading artifact</i></p> <p>Occurs when radiofrequency pulses are applied at flip angles other than 90 and 180 degrees and causes uneven excitation of nuclei inside the magnetic field [27]</p>
MRI		<p><i>Zero fill artifact</i></p> <p>If K-space array data is missing at some point during scanning, the abrupt signal changes from no signal to existing signal creates the zero fill artifact [33]</p>

1.5. Magnetic susceptibility and permeability

The induced field (B) and applied field (H) are almost identical when there is no matter is present throughout MRI. When matter is present in a given region of space, multiple electromagnetic interactions take place that focus or scatter the magnetic lines of force [8, 9]. As a result, the induced field (B) is generally never directly proportional to the applied field (H). Magnetic susceptibility (χ), also known as magnetisability, is a one-dimensional constant, which is proportional to the applied field [36, 37]. When subjected to an external magnetic field, it is a measurement of how much a substance magnetises. Another dimensionless constant is magnetic permeability, which is considered a physical constant. Magnetic effects may be found in three types. Almost all biological tissues are diamagnetic in a weak way. Except for minuscule amounts of magnetite, the human body has no endogenous ferromagnetic substances [37]. In contrast, most extrinsic metallic foreign entities and implanted devices seen in magnetic resonance imaging are ferromagnetic [9, 38, 39].

Table 8. Material classification based on interactions with magnetic field [40]

Type of magnetic effect	Effect on applied magnetic field	Magnetic permeability/susceptibility	Significance	Example
Diamagnetism	Internal magnetization opposes the applied external field. Magnetic field lines are spread or thinned.	$\mu < 1$ (or $\chi < 0$)	Unlikely to cause an artifact	All biological tissues; Ceramics
		Slightly lower permeability than free space; Negative susceptibility		
Paramagnetism	Magnetic field lines are focused in the item; internal magnetization is in the same direction as the externally applied field.	$\mu > 1$ (or $\chi > 0$)	Least likely to cause an artifact	Titanium alloys; Aluminium
		Slightly higher permeability than free space; Positive susceptibility		
Ferromagnetism	Magnetic field lines are concentrated in the object; Strongly attracted by a magnetic field	$\mu \gg 1$ (or $\chi \gg 0$)	High potential to cause MRI artifacts	Stainless steel
		High permeability; Positive susceptibility		

The greater a material's magnetic permeability, the bigger the magnetic field distortion (the magnitude of the resulting artifact) [40]. As a result, alloy composition is significant in the formation of MRI artifacts. Other critical considerations include the metallic material's size and form, including its location inside the body. Even when in close vicinity to dental materials with low magnetic susceptibility, magnetic resonance imaging without artifacts is possible (precious metal alloys and titanium) [41]. Regrettably, not all current dental materials meet this low magnetic susceptibility requirement. (Table 8) [37, 40, 41].

Table 9. Listing of orthodontic appliance compatibility with magnetic field [14] Δx – susceptibility difference between susceptibility of material and susceptibility of water. SE – Spin Echo, GRE – Gradient Echo. [37]

Classification	Description	Significance	Example
Compatible	Compatible: $\Delta x < 3$ ppm	Fully compatible materials;	Resin-based sealer, zirconium dioxide, glass ionomer cement
	Material produces no detectable distortions on either SE or GRE imaging	Can be present even in the location of interest.	
Compatible I	Compatible I: $3 < \Delta x < 200$ ppm	Limited distortions;	Gold alloy, amalgam, gold-ceramic crowns, NiTi orthodontic wires, titanium alloy, aluminium
	The material causes significant distortions; acceptability is determined by the application.	Image usability and interpretability depends on area of interest	
Non-compatible	Non-compatible: $\Delta x > 200$ ppm	Strongest distortions	Stainless steel orthodontic appliances (wires, brackets)
	Even when the material is placed far away from the imaging field, it creates significant image distortions.	Classified as non-compatible	

1.6. Artifact reduction methods in MRI

In MRI there are a total of three methods used for artifact reduction, which include View angle-tilting (VAT), Multi-acquisition variable resonance image combination (MAVRIC) and Slice Encoding for Metal Artifact Correction (SEMAC) [42, 43]. When it comes to correcting in-plane distortions, a technique known as view-angle tilting (VAT) can be quite effective. VAT makes use of the fact that the slice displacement and in-plane displacement created due to off-resonance are both widely defined and also have a fixed value [3, 8]. VAT replicates the slice-selection gradient which shears the image during the readout. As a result, in-plane displacements are nullified, and in-plane displacements are eliminated. VAT, on the other hand, by itself doesn't fix the slice distortion. Another interpretation of VAT is that the radiofrequency stimulates a specified bandwidth. Off-resonance is restricted to the RF bandwidth and in-plane distortion is nearly removed by repeating the slice selection gradient. The disadvantage of VAT is that the readout length is restricted to those from the radiofrequency excitation, which might produce blurring. This reduces the SNR resolution or spatial resolution that could be attained [44]. When utilising VAT, a high bandwidth readout is essential for preventing blurring and eliminating residual effects from tilting the voxels. This is made possible by spectral-spatial excitation, which stimulates both a limited and a limited frequency band. Because the frequency range is short, the in-plane artifact is limited. The disadvantage of this approach would be that the excitation should be done for each frequency, which in reality increases scan time duration. [42, 43].

MAVRIC is an approach to solving displacement artifacts in both in-plane and through-slice. Frequency-selective excitation while using MAVRIC limits the number of frequency offsets imaged at one at a time [42, 8]. This is then followed up by a standard 3-dimensional image readout, which is commonly done with a spin echo train. While its frequency range is reduced, the in-plane displacement is usually less than a pixel [43, 44]. MAVRIC prevents slice-direction dislocation by

resolving them in this direction utilising phase encoding. The 3-dimensional images are then replicated for a number of frequencies and then aggregated using a sum-of-squares algorithm. The combined images have less artifacts and offer a signal from a variety of near-metal frequency offsets [44, 45].

The SEMAC approach, like MAVRIC, fixes artefacts created by metal objects by effectively encoding each excited slice against metal-induced field inhomogeneities. That way, SEMAC can correct in-plane and through-slice artifacts [42, 43]. The view-angle tilting (VAT) spin-echo (SE) series is strengthened with extra z-phase encoding to provide robust slice encoding. But even though the VAT correction gradient eliminates most in-plane distortions, z-phase encoding entirely eliminates distorted excitation patterns that cause through-plane distortions. By summing up the fixed spins in each voxel, through-plane distortions could well be corrected by aligning all spins in a region of interest to their correct spatial locations [46, 47]. The SEMAC approach requires no new additional hardware and is compatible with a wide range of full-body MRI devices. The SEMAC method's efficiency in reducing metal-induced artifacts while maintaining tolerable scan time durations [47, 48].

1.7. Artifact reduction methods in CT

Metal induced artifact reduction solutions focus on minimising all of the artifact's principal causes, which include beam hardening, photon hunger, scatter, noise, edge effects, and the combined effect. The methods adopted fall into three categories: 1) adjusting conventional acquisition and reconstruction, 2) modifying projection and/or image data, 3) dual-energy CT applications (DECT) [8, 39].

Increasing the kVp and mAs is a traditional way for lowering the amount of metal artifacts. More photons will reach the detector when the average photon energy is increased by increasing kVp, since lower energy photons are much more easily attenuated by metal objects than high-energy photons with greater penetration. Increasing the mAs value also boosts the number of photons that reach the detector, reducing noise and photon-starvation [50, 51]. Slightly less overall collimation, or detector width, minimises scattering. Using an extended Hounsfield Unit (HU) scale and a soft reconstruction kernel rather than a bone kernel after image capture reduces the visual predominance of metal induced artifacts. [51, 52]

The Metal Artifact Reduction (MAR) algorithm is used to change the projection and/or image data. Each vendor does have its own modified and protected version of MAR (iMAR (Siemens), O-MAR (Philips), SEMAR (Toshiba/Canon), SmartMAR (General Electric)), but the underlying technology remains the same [50]. The core of MAR methods is the in-painting approach, which identifies distorted projection data caused by the presence of metal and then replaces this distorted projection data with averaged or interpolated data from nearby detector components. An unadjusted image is constructed utilising CT projection data or a sinogram to do this. The metal implant affected image is then generated using thresholding [50, 52]. Any pixels with a higher value are presumed to be from the metal CT image throughout this technique. A metal sinogram is created by projecting the metal image forward and merging it with the original sinogram. Back-projecting the revised sinogram yields a rectified picture that may be used as a starting point for further changes [51]. Because of the limitations of thresholding, this method reduces metal induced artifacts while simultaneously introducing new artifacts, resulting in an insufficient new sinogram. [50, 52].

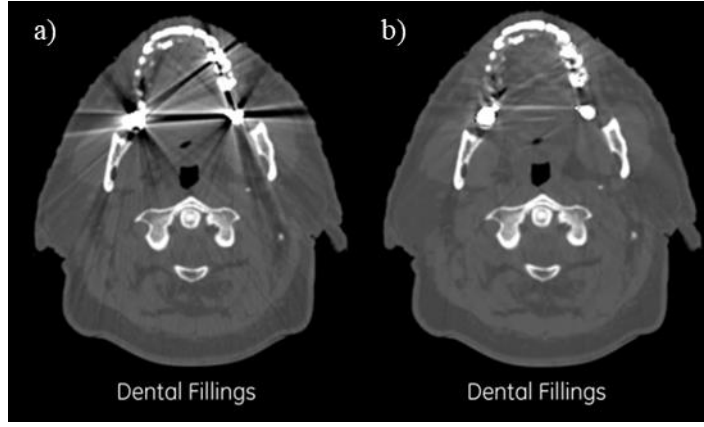


Figure 1. Head CT with dental fillings before (a) and after (b) the use of MAR [53]

As a result of recent breakthroughs in artificial intelligence, deep learning (DL) has acquired favour in the field of medicine. Image-based MAR algorithms have largely employed DL in CT. The bulk of DL-MAR algorithms require paired data and are supervised. The difficulty of collecting data from real patients is a major limitation of supervised techniques. To deal with this problem, generative adversarial networks (GANs) have been extensively studied as a cornerstone for unsupervised techniques [54]. The GAN is a generative model designed to generate samples directly from a distribution of data without explicitly modelling the underlying probability density function. A generator G and a discriminator D are the two neural networks that make up this system. For simplicity, the input to G , z is pure random noise taken from a previous distribution $p(z)$, which is generally chosen to be a Gaussian or uniform distribution [54, 55]. G 's output, x_g , is anticipated to be visually comparable to the genuine sample x_r selected from the genuine data distribution $p_r(x)$. The nonlinear mapping function learnt by G and parameterized by θ_g is denoted as $x_g = G(z; \theta_g)$. D accepts either a real or created sample as input. D , y_1 returns a single value indicating if the input is a legitimate or a false sample. $y_1 = D(x; \theta_d)$ denotes the mapping learnt by D and parameterized by θ_d . Following successful training, the generated samples form the $p_g(x)$ distribution, which is meant to approximate $p_r(x)$. Equation 1 and 2 shows how D and G 's training objectives may be stated mathematically [54, 55, 56]

$$\mathcal{L}_D^{GAN} = \max_D \mathbb{E}_{x_r \sim p_r(x)} [\log D(x_r)] + \mathbb{E}_{x_g \sim p_g(x)} [\log(1 - D(x_g))], \quad (1)$$

$$\mathcal{L}_G^{GAN} = \min_G \mathbb{E}_{x_g \sim p_g(x)} [\log(1 - D(x_g))]. \quad (2)$$

GAN-based MAR algorithms for images with metals have recently attracted a lot of attention in diagnostic radiology. In therapeutic radiology, a two-dimensional (2D) cycle-consistent GAN (CycleGAN)-based MAR method in intensity-modulated radiation for patients with dental fillings has been suggested [56]. By eliminating manual demarcation and maintaining consistent dosage distribution against metal artifacts, this highlighted the planning method' efficiency. However, their conclusions were based on 2D research using artifact-corrected CT volumes and the water density override method [56, 57]

Dual energy CT can reduce metallic artifacts by reconstructing the images acquired with two photon spectra at different kVp's. Fast kV-switching of tube voltage, multiple tubes, a dual-layer detector, or a beam split filter are used to generate the spectra [58, 59]. There are two methods for recreating a picture once the projection data has been recorded. The first technique generates virtual

monochromatic images by reconstructing them from two sets of projection data recorded and processed at the same time. The other technique generates virtual monochromatic images in the image domain by reconstructing images at the two kVp levels separately [58]. Because virtual monochromatic images depict reconstructions at arbitrary average energies, they may be used to optimize contrast and reduce artifacts. Extrapolating to higher virtual monochromatic energies reduces the effects of low-energy photons, resulting in fewer beam hardening artifacts [60, 61].

1.8. Artifact reduction methods in US

The physical characteristics of ultrasound, such as beam generation, sound propagation through matter, sound engagement with reflecting surfaces, and echo detection and processing are used to create a US picture [6, 62]. The position and strength of each received echo are assigned using physical presumptions by ultrasound display devices. These presumptions are based on that the speed of sound in human tissue is constant, the sound beam and its echo travel in a straight path, and the acoustic energy in an ultrasound field is uniformly attenuated [6, 63]. These assumptions are frequently disregarded in clinical sonography and as a result, echoes may be shown incorrectly, and mistakenly as artifacts [62, 63]. Artifacts appear as a result of inaccuracies caused by ultrasound beam properties, various echo routes, attenuation problems and velocity errors.

Morphological image processing (MIC) is a method of altering a picture's pixels. The pixels in a grayscale image are distinguished by binary values of 0 and 1, and the procedure is carried out by using either complex image processing algorithms or straightforward mathematical calculations [6, 63, 64]. Erosion and dilation, as well as opening and closure, are a few examples. The main objective of morphological image processing is to get rid of undesirable artefacts and increase medical image quality. In an image, an object is represented by a specific group of pixels known as object pixels. Background pixels are usually depicted as white and are shown individually. Erosion turns pixels linked with the object's boundaries to background pixels, whereas dilatation changes bordering background pixels to those linked with the object [64, 65]. Objects diminish during the erosion process and increase in size or even fuse during the dilatation process. In morphological image processing, the two techniques may be combined to alter an image by performing erosion and then dilation, which results in opening. To smooth up the image, filaments and isolated pixels can sometimes be deleted from the object in this way. The closure operation can be used to filter background pixels by removing gaps and pixels that were previously known to be out of place. Skeletonization is a morphological image processing method in which superfluous pixels are deleted in order to generate single lines [6, 64, 65, 66].

Table 10. Comparison of artifact reduction methods in MRI, CT and US systems [3, 6, 8, 43, 44, 56, 57, 60, 61, 63, 64]

Method	Advantages	Disadvantages
VAT (MRI)	Is integrated in almost every diagnostic MRI; Cancels in-plane displacements at the cost of slightly tilted images.	Unable to fix through-plane slice distortions, therefore signal pile-up's may occur near metallic implants; Produces blurring.
MAVRIC (MRI)	Excited limited frequency bands; Using phase encoding avoids slice-direction displacements; Minimal artifacts, includes signals from offsets near metal.	Generates a lot of heat (Specific Absorption Rate) in metallic implant, which leads to probability of scan inhibition;
SEMAC (MRI)	Excites limited spatial bands; Metallic implants can be seen almost clearly without distortion or pile-up artifacts.	Might create "potato-chip" artifact on soft tissues at the cost of better visualisation on prosthesis or implant.
kVp and mAs increase (CT)	kVp increase: high energy photons won't be easily attenuated by the metallic implant; mAs increase: lowers the noise and photon-starvation, therefore more photons will reach the detector.	Higher dose received by the patient; Is not as effective as MAR or DECT methods.
MAR (CT)	Thresholding; Produces and compares two sinograms (original and corrected); Combines both sinograms to create an image with fewer artifacts.	Constraints of thresholding can introduce new artifact, due to inadequate sinogram.
DECT (CT)	Two photon spectras at different kVp's; Lower kVp image is used to optimize contrast and reduce artifacts; Higher kVp image reduces beam hardening and metallic artifacts.	Long reconstruction times (~5min.); Very sensitive to motion artifacts and noise. Reduced effect on metallic implants with higher molecular weight and bigger size.
MIC (US)	Wide variety of filters to achieve efficient and effective denoising.	Requires external hardware and software to properly denoise the image, and knowledge of how to implement variety of filters.

1.9. Medical implant materials

Minerals and metals are crucial parts of medical equipment that enable millions of people to live healthy lives. Implanted devices in the human body can replace, support, or improve an existing bodily component [67, 68]. Numerous different devices are capable of diagnosing, monitoring, and treating clinical diseases, therefore saving lives and increasing people's quality of life. There are several medical devices available, each with its own set of materials and unique properties. Main properties of each material are divided into three categories: bulk properties, surface properties and biocompatibility [67, 68, 69].

Bulk properties require the materials to have high modulus of elasticity, where implant material must have an elasticity value comparable to bone. Shear strength and fatigue strength require the implant to be resistant to fractures under cyclic loadings. Ductility in implant is necessary for

shaping and contouring of implant [70]. Ductility is the most important factor in orthodontics. Last bulk characteristic is hardness and toughness, which determines the rate of wear of the implant and prevents fractures [68, 69].

Surface properties consist of surface tensions and/or surface energy, which determines the wettability of implant by wetting fluids and adsorption of proteins. Surface roughness is also present in surface properties and leads to changes within surface roughness of implants affect cell and tissue response by increasing the surface area of the implant in near proximity to bone and so enhancing cell adhesion to the bone [67, 71]. Different criteria, namely as roughness, texture, and irregularity of orientation, have been used to classify implant surfaces. Surface morphology of implant surfaces is being classified as minimally rough (0.5-1 μm), intermediately rough (1-2 μm), or rough (2-3 μm) [71, 72]. The texture of the implant surface can alternatively be characterised as concave texture or convex texture. Lastly, the orientation of surface imperfections on the implant surface may be classified into isotropic surfaces that have a same topology regardless of measurement direction, and anisotropic surfaces, which feature distinct directionality and a broad range of roughness [68, 69, 71].

Biocompatibility is the ability of a medical implant material to respond favourably in a certain biological environment in a specific purpose. Mostly it depends on corrosion resistance, crevice corrosion, omitting corrosion, galvanic corrosion and electrochemical corrosion, which means that corrosion resistance is mandatory for implant biomaterial as corrosion can cause surface roughening, weakness to restoration, chemical components release from the metal or alloy, and adverse reactions [67, 68, 71]. Adjacent tissues could become discoloured, and patients might experience allergic responses as a result of chemical component release. The most popular medical implant materials are stainless steel, zirconia ceramics, aluminium and titanium alloys (Ti 6Al 4V) [71, 72].

1.9.1. Stainless steel

Stainless steels are often the primary metallic materials utilised in medical devices. Stainless steels used for medical devices ought to have exceptional mechanical qualities such as hardness, tensile strength, wear resistance, fracture toughness, elongation, and creep resistance, among others. All of these attributes are accomplished by integrating the charge materials' characteristics with the elaboration methods [73]. Approximately one percent of total of stainless steel output is utilised in medical applications, such as tools and surgical components, necessitating its increase [73, 74]. Despite this, there are exceptions to the general rule, which are enforced by special criteria for resistance to corrosion, as well as the amount and size of permitted impurities [75, 76]. The stainless steels family for medical devices may be classified in a variety of approaches, but the one that most accurately describes metallographic structure appears to include ferritic steels, austenitic steels, martensitic steels, and duplex steels (ferrite and austenite mixture) [74, 77]. The chemical composition, also known as alloying degree of these steels, as well as the thermal and mechanical treatments used, determine how steels are made. The primary purpose of alloying elements is to increase resistance to corrosion while also enhancing mechanical and physical qualities. The alloying elements can be alphas (Cr, Mo, Si, Ti, Nb) and gammas (C, Ni, Mn, N) in order to increase the spacing of solid solution [73, 75, 77]. The structure of stainless steel is usually determined by the presence of alphas and gammas components in its composition (Figure 2) [73, 78].

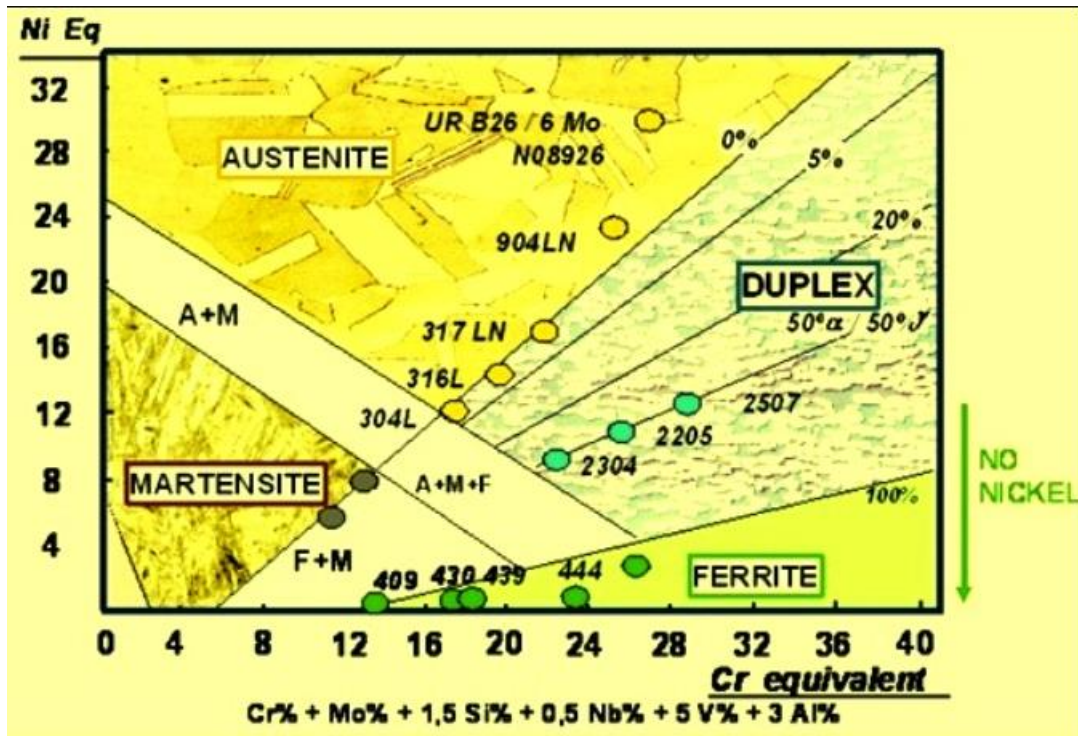


Figure 2. Schaeffler diagram for stainless steels [78]

Table 11. Differences between Austenitic stainless steels and Martensitic stainless steels [76, 77]

Dimensions	Austenitic Stainless Steel	Martensitic Stainless Steel
Definition	Austenitic stainless steel is a type of stainless steel alloy that has excellent resistance to corrosion as well as outstanding mechanical characteristics.	Martensitic stainless steels contain greater amount of chromium and, primarily, no nickel
Composition	Major ingredients include iron, chromium, nickel, and carbon.	Iron, chromium and carbon
Nickel	Contains about 8 to 10% nickel	Contains no nickel
Magnetic Properties	Diamagnetic	Ferromagnetic
Applications at high temperatures	Can be used at both low and high temperatures.	Cannot be used at high temperatures.
Crystal structure	Face-centered	Body-centered
Corrosion resistance	Exceptional corrosion resistance	Marginally less corrosion resistance

ISO 7153-1/1991 outlines typical stainless steel categories used for surgical and dental instruments used globally, as well as usage guidelines. Austenitic and martensitic stainless steels are hence the most often utilised stainless steels for medical equipment. Austenitic stainless steels have low carbon content (0.1%), a composition of 12-25% Cr, and a content of 8-30% Ni, and exhibit austenitic stability until cryogenic temperatures [73, 76]. Such steels offer excellent mechanical characteristics, such as resistance to corrosion, ease of processing through plastic deformation, and good welding behaviour, but they come at a premium price. The poor corrosion resistance of austenitic stainless steels under strain limits their practical use, especially in chloride solution conditions at high temperatures [77]. Austenitic stainless steels are used in medical devices that require reduced resistance to corrosion, such as cannulas, containers, dental impression trays, steam

sterilisers, hypodermic needles, storage cabinets and workstation tables etc. Martensitic stainless steels are most commonly distinguished by a high chromium concentration, consisting of 12-17% and a higher carbon content of above 0.1%. In certain situations, the carbon concentration can reach 0.4-0.5%, and in exceptional circumstances, 1.0%. Silicon might be added to strengthen their resistance to heat oxidation, and they are alloyed with 2-4% Ni to improve toughness [73, 75]. Titanium may be also present in some martensitic stainless steels. Surgical and dental instruments are frequently made of martensitic stainless steels. Heat treatment could also be used to harden and temper such stainless steels. As a result, they would generate a wide range of mechanical qualities, including increased hardness for cutting instruments such as scalpels, forceps, chisels, dental pliers, and etc. Ferritic stainless steels are used for a limited number of medical instruments, such as solid handles for guiding pins and forceps. Duplex stainless steels have yet to have a substantial influence on the medical field [74, 76, 77].

1.9.2. Aluminium

Aluminium is mostly used as a part of titanium alloys (Ti 6Al 4V and Ti 6Al 7Nb) or as a sandblasting and acid-etching process (Al_2O_3), which coats the implant for increased biocompatibility [79]. Dental implant surfaces play an important role in osseointegration and therefore remain to be the focus of biomedical research into how surface alterations impact osteogenic capability. Dental implants had largely machined surfaces in the early decades after their debut, which were made using turning, milling, or polishing procedures [80]. Even though manufactured implants have a good long-term rate of survival after osseointegration, they need a somewhat longer recovery period of 3 to 6 months based on anatomical location and bone quality, and they have a relatively high chance of premature failure [79, 80].

Titanium alloys have excellent mechanical qualities as well as biocompatibility and resistance to corrosion, making them ideal for medical applications. For example, Commercially pure titanium (CP-Ti) and Ti 6Al 4V are frequently utilised in the manufacture of implants [80]. Because vanadium is poisonous and can harm the human body, Ti 6Al 7Nb was created on the basis of Ti 6Al 4V to combat the potential negative health consequences of this alloying element. Al is also a confirmed harmful element that has been linked to Alzheimer's disease. Aluminium chloride has also been shown experimentally in animal cancer models to induce breast cancer. As a result, the high Al concentration of Ti 6Al 4V and Ti 6Al 7Nb is cause for concern, and long-term unfavourable health consequences cannot be ruled out [79, 80].

1.9.3. E-max

Lithium disilicate glass ceramics (LDGC), also known as Emax crowns, are cosmetic dental products manufactured from $\text{SiO}_2\text{-Li}_2\text{O-Al}_2\text{O}_3\text{-K}_2\text{O-ZrO}_2\text{-P}_2\text{O}_5$ glass systems by a method of solid-state reaction [81]. LDGCs are noted for their excellent durability and are the oldest known dental repair technology. LDGC contains 70% lithium disilicate ($\text{Li}_2\text{Si}_2\text{O}_5$) crystals contained in a matrix mostly composed of SiO_2 , Li_2O , Al_2O_3 , K_2O , P_2O_5 , and various oxide replacements similar to a needle-like structure [82]. The diameters of the $\text{Li}_2\text{Si}_2\text{O}_5$ crystals reinforced in the glassy matrix are only a few microns, and the architecture is interlocking, enabling high tensile strength of 360–400 MPa [81]. LDGCs are ideal materials for dental implants due to their chemical stability, appealing nature, and improved optical translucency [81, 82].

1.9.4. Zirconia

High strength zirconia ceramics have been popular as novel materials for dental implants in recent years. They are thought to be inert in the body and exhibits way less ions than metal implants [83, 84]. Because of their superior fracture resistance and flexural strength, yttrium-stabilized tetragonal zirconia polycrystals appear to provide benefits over aluminium oxide for dental implants. They've been also utilised effectively in orthopaedic surgery to make sphere heads for complete hip replacements, which has been the biomaterial's primary application today [81, 82, 84]. Because of its toothlike colour, mechanical qualities, and hence biocompatibility, zirconia appears to be a viable dental implant material. Implant-related apical bone loss and gingival recession frequently expose sections of the metal implant, showing a bluish colour of the underlying gums [82, 83].

Thus, the usage of zirconia implants prevents this problem and fulfills to many patients' requests for metal-free implants [83, 84]. In addition, the material has great fracture toughness, strength, and biocompatibility. The inflammatory reaction and resorption of the bone caused by ceramic particles are lower than those induced by titanium particles, indicating that ceramics are biocompatible [81, 83, 84].

1.9.5. K

Leucite is a feldspathoid rock-forming mineral that is silica-undersaturated and made up of potassium and aluminium tectosilicate $K[AlSi_2O_6]$ and it is a key crystalline component of dental porcelains [85, 88]. Tetrahedral leucite enhances overall coefficients of thermal expansion of dental porcelains due to its high coefficient of thermal expansion. This seems to be especially beneficial for porcelains that are designed to bond to precious metals and alloys [86]. Dental porcelain is obtained by increasing K_2O (potassium oxide) concentration in alumino-silicate glass. Glass-ceramics made of leucite are extremely biocompatible [87]. Aside from its excellent physical, chemical, and mechanical qualities (Table 12), this type of glass-ceramic is ideal for computer aided machining. This form of glass-ceramic is made using a technique that controls the nucleation and crystallisation process of a base glass [86, 88].

Table 12. Comparison of mechanical, physical and chemical properties of K and Emax samples [81, 82, 87, 88]

Properties	Units	K	Emax
Biaxial flexural strength	MPa	160	300-420
Fracture toughness	$MPa \cdot m^{1/2}$	1.3	2.0-2.5
Hardness	MPa	6200	5700-5900
Elastic modulus	GPa	62	90-100
Coefficient of thermal expansion	$10^{-6} K^{-1}$	17-18	10.2-10.7

2. Materials and methods

Experiments were performed on a Varian Medical Systems VISION 3253S2 CBCT (6 MV and 125 kV) system, Siemens MAGNETOM Amira 1.5 T with head coil and Sag T1 TSE sequence, and an U5 Harmonic ultrasound machine with two different frequency probes of 6.5 MHz and 7.5 MHz (figure 3).

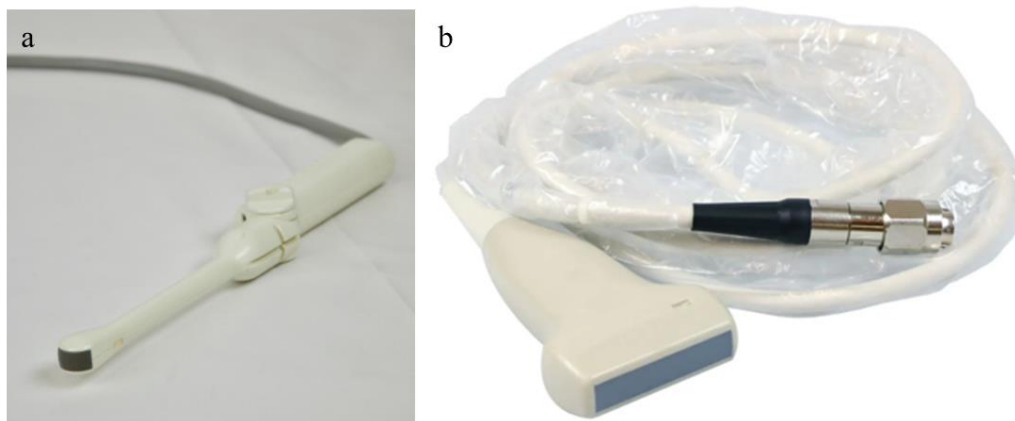


Figure 3. US 6.5 MHz rounded probe (a) and 7.5 MHz linear probe (b) [97, 98]

Samples were obtained in accordance to materials, which are most commonly used in medical implants and shaped to be in somewhat similar size. Five samples in total were chosen and included stainless steel (**SS**) (3 cm x 1 cm 0.1 cm), aluminium metal (**Al**) (3 cm x 1 cm 0.1 cm), and three types standard filling/dental prosthesis materials from Zr series, K series and E-max series. **Zr** series Katana Zirconia STML (1.3 cm x 1.25 cm x 0.1 cm) made from transparent multi-layer zirconium dioxide and chemical composition ZrO_2+HfO_2 (88-93%); Y_2O_3 (7-10) %; other oxides (0-2%). **K** series ENAMEL plus HRi biofunction (MICERIUM S.p.A, Italy) ($r = 1.8$ cm x 0.1cm) is a composite material which is obtained by UV beam hardening with main chemical components urethane dimeticrilate, tricycle decane dimethanol dimeticrilate and filling consisting of silica dioxide particles (0.005 μm) and glass particles (0.2-3 μm). **E-max** series Ivoclar Vivadent IPS E.max press (1.3 cm x 1.1 cm x 0.1 cm) lithium disilicate-enriched pressings glass ceramics with a chemical composition of SiO_2 (57-80) %, Li_2O (11-19) %, K_2O (0-13) %, P_2O_5 (0-11) %, ZrO_2 (0-8) %, ZnO (0-8) %, other oxides: Al_2O_3 , MgO , La_2O_3 and pigments (0-10) %. In order to properly image the samples a special sample holder, which would not obstruct the irradiation process (CBCT kV and MV) of the sample and would not produce any additional artifacts when imaging, (Figure 4) was 3D modelled with 3D printer Zotrax M300. The samples were then imaged while submerged in water for MRI, US and CT, while CT imaging was also performed without water [91, 92, 93, 94]. T1-weighted imaging was chosen due to the fact that short TE and TR timings are used to generate T1-weighted images [90]. The image's contrast and brightness are mostly governed by the T1 characteristics of the tissue. T2-weighted pictures, on the other hand, are created by employing longer TE and TR periods. The contrast and brightness of these pictures are mostly governed by the T2 characteristics of the tissue. T1-weighted imaging can also be conducted with Gadolinium injection. Gadolinium is a non-toxic paramagnetic contrast enhancer. When gadolinium is injected during the scan, it reduces signal intensity by shortening T1. As a result, gadolinium appears particularly bright on T1-weighted imaging [89]. Thus the T1-weighted imaging sequence is extremely valuable in diagnostic imaging and is more susceptible to artifacts due to incompatible medical implants. Image J software was used for evaluation of images by contouring the artifact

size and determining the affected area in US images [96]. 3D Slicer software was used for CBCT and MRI artifact volume determination with the usage of thresholding and 3D modelling. Also, contrast to noise ratio (CNR) was calculated by measuring a fixed size field (ROI) of 10 cm x 10 cm on the image where no artifact (background) was present and then in a location where artefact and background was present [95].

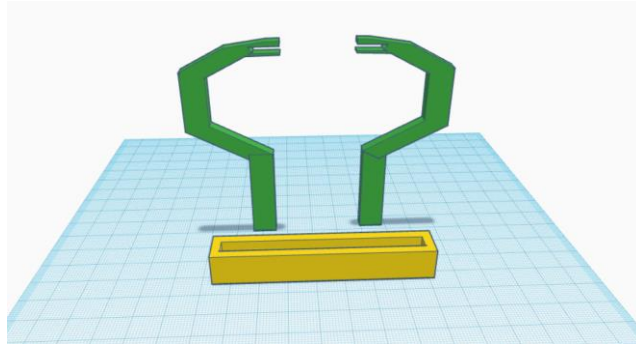


Figure 4. 3D modelled sample holder



Figure 5. Upper image: Ivoclar Vivadent IPS E.max press (E-max), Katana Zirconia STML (Zr) and ENAMEL plus HRi biofunction (K) samples; Image on the left: E-max sample atomic force microscopy image [99]; Image on the right: Zr sample atomic force microscopy image [100].

3. Results

After performing sample (Figure 6) imaging with MRI, CT (Table 15) and US (Figure 9 – 18) medical imaging modalities, the Image J and 3D Slicer analysis (Figure 7-8) presented the following results:



Figure 6. Prepared samples for imaging without adding water

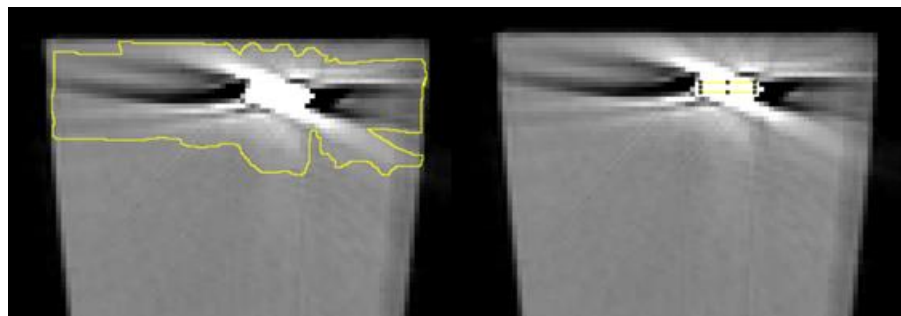


Figure 7. Measuring the affected artifact area with Image J by contouring the artifact and subtracting the implant material.

Artifactual volume calculations were performed in a specific workflow with 3D Slicer application, which is presented below. All of the sample images underwent the same workflow, but as an example, the CBCT kV without water Zr sample is shown. Due to barely noticeable difference the human eye cannot correctly differentiate the grayscale image between the artifact and sample itself, as both of them are purely white. That is why, 3D Slicer application applied thresholding to exclude the sample material itself out of volume calculations, because in reality the sample had higher grayscale values than the artifact. Furthermore, after cutting the unnecessary parts of the 3D model, only the artifact volume remained for calculations.

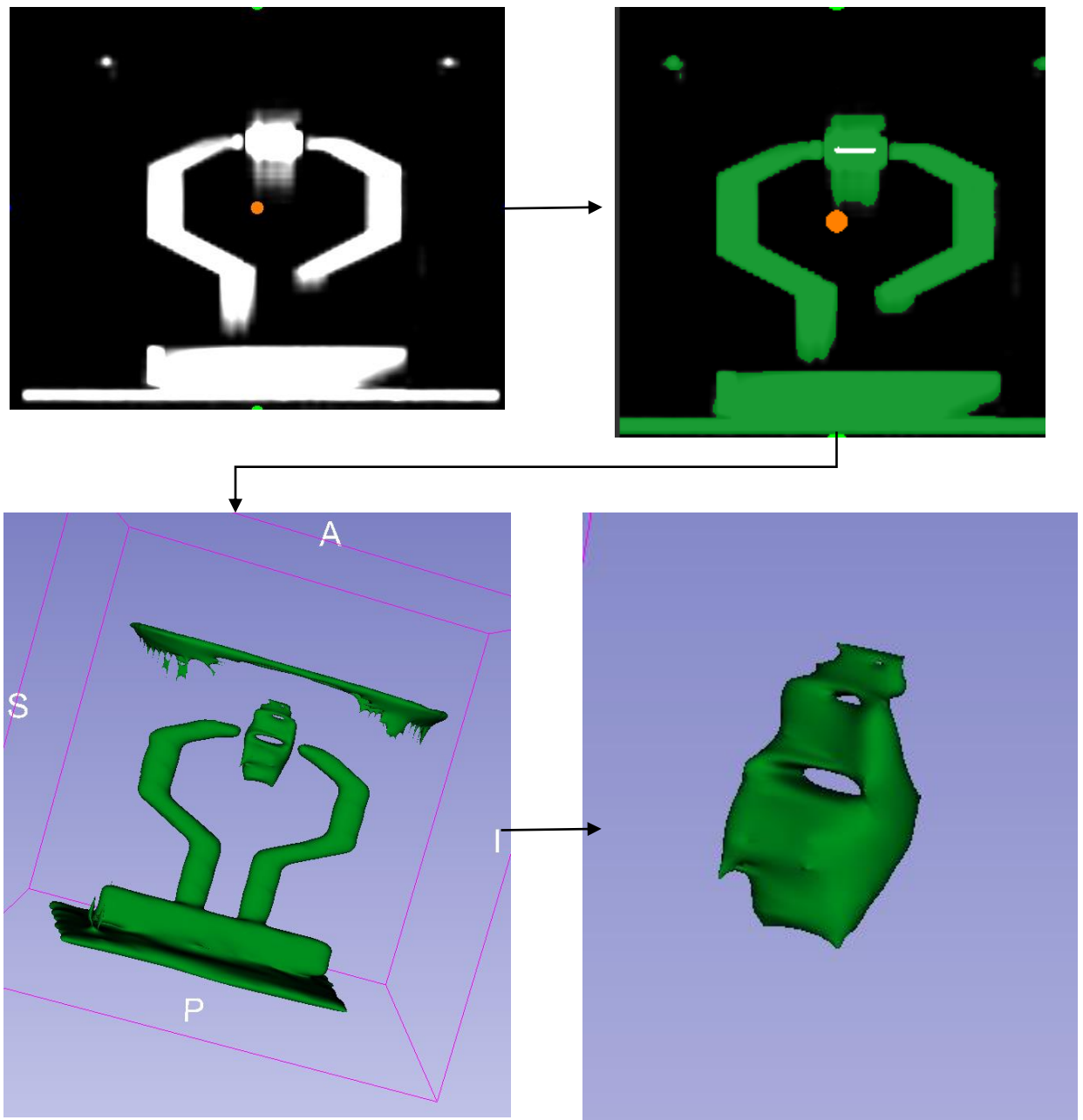


Figure 8. Workflow of artifacting volume determination of CBCT kV without water Zr sample while applying thresholding in 3D Slicer application

3.1. CBCT and MRI artifacting results

According to table 13 presented below, in CBCT imaging, the most affected volume of the artifact was found in CBCT kV imaging while samples were submerged in water, where Zr sample exhibited the greatest image distortion (16720.87 mm³), and aluminium sample provided the smallest distortions as the artifact volume was only 3344.54 mm³. CBCT kV without water and CBCT MV imaging with and without water presented much lower image distortions, compared to CBCT kV with water. On other hand, CBCT kV imaging without water showed higher artifact volumes for Zr (3282.44 mm³) and stainless steel (6224.28 mm³) samples, but the artifact volume of K (266.793 mm³), E-max (610.956 mm³) and aluminium (1410.44 mm³) samples was lower when compared to CBCT MV imaging with water. Overall, CBCT MV imaging is less susceptible to artifacts, than CBCT kV imaging, but the best results would be achieved in CBCT imaging without water, yet in reality it is impossible due to the fact, that mostly humans are being imaged and they are made mostly out of water.

Table 13. Artifact affected volume in CBCT kV and MV with water and without


























CBCT	With H ₂ O kV	Without H ₂ O kV	With H ₂ O MV	Without H ₂ O MV
Sample	Artifact volume, mm ³			
Zr	16720.87	3282.44	1727.94	419.245
Stainless steel	12540.62	6224.28	1478.58	1074.75
K	6855.21	266.793	896.396	301.115
E-max	8527.29	610.956	889.447	430.826
Aluminium	3344.54	1410.44	1994.31	365.97

Table 14. Artifact affected volume in MRI with Sag T1 TSE sequence with water

MRI	Sag T1 TSE
Sample	Artifact volume, mm ³
Zr	362.973
Stainless steel	25493.33
K	188.894
E-max	883.357
Aluminium	2400.07

In MRI imaging the biggest artifact was exhibited by stainless steel sample (25493.33 mm³), as it is a ferromagnetic material, has high electroconductivity and low thermal conductivity (15 W/mK), therefore distorts the image the most. Aluminium is also a ferromagnetic material, has high electroconductivity, although it is less electroconductive than stainless steel, but has better thermal conductivity (237 W/mK), therefore it produced lower artifact volume of 2400.07 mm³ in comparison to 25493.33 mm³ of stainless steel. Out of dental implant materials/dental filling of Zr, K and E-max samples, the latter one showed the biggest artifact volume of 883.357 mm³, where Zr and K artifact volumes were 362.973 mm³ and 188.894 mm³, respectively. Overall, MRI is the best modality for people with dental implants/dental filling made out of Ivoclar Vivadent IPS E.max press (E-max), Katana Zirconia STML (Zr) or ENAMEL plus HRi biofunction (K) samples, as they produce the least amount of artifacts.

Table 15. View of the biggest artifacting area of each imaged sample in CBCT and MRI modalities

Sample	CBCT kV w/o H ₂ O	CBCT kV with H ₂ O	CBCT MV w/o H ₂ O	CBCT MV with H ₂ O	MRI
Zr					
SS					
K					
E-max					
Al					

3.2. US artifacting results

Artifacts in US imaging are different due to unique interactions between sound and imaged material, as materials density and surface plays an important role. Higher density materials lead to increased chance of the appearance of reverberation artifact, whose intensity is determined by the frequency of the probe, density and surface of the examined material. Higher frequency probes produce high resolution images, but are only usable in surface examinations, whereas lower frequency has greater penetration, but lower resolution. 7.5 MHz imaging of Zr, stainless steel, E-max and aluminium samples produced the reverberation artifact, as seen in [14], but with different intensities. Stainless steel sample produced the largest reverberation artifact combined with follow-up noise with an artifact area of 70550 mm², where aluminium, E-max and Zr samples created smaller reverberation artifacts by a large margin, 34818 mm², 26749 mm² and 22659 mm², respectively. Artifact area is the largest for stainless steel as the material has the highest density among other samples. The K sample in 7.5 MHz imaging exhibited a different type of artifact (Figure 13), called acoustic shadowing, which was mentioned in literature review [19]. This artifact appeared as sound waves were not able to pass through the sample, thus creating a shadow. Acoustic shadowing does not “distort” the image, but prevents the visualisation of object behind the implant.

While imaging the samples with 6.5 MHz probe, the Zr sample produced only noise, also known as speckle artifact [15, 20], which in reality is quite common and nearly impossible to remove. Stainless steel sample exhibited a sub-type of reverberation artifact, named ring down artifact (Figure 12), which was discussed in the literature review [16]. Ring down artifact is rare as it requires extremely specific circumstances in order to appear. This artifact occurs when the sound wave is trapped between 4 air bubbles on the examined surface, where three bubbles are on top and one is nestled deep to them. The trapped bubbles on the surfaces resonate and emit a continuous signal back to the probe. Aluminium and E-max samples produced the same reverberation artifact in 6.5 MHz imaging, but artifact created by aluminium (30121 mm²) was larger than E-max (9487 mm²). The K sample in 6.5 MHz imaging created the same acoustic shadowing artifact as in 7.5 MHz imaging, just in a larger size of 14873 mm², compared to 7512 mm². While comparing the

surfaces of Zr and E-max sample, it was noted that Zr sample has a smoother surface (Figure 5) when analysed with atomic force microscopy, compared to E-max thus rougher surface material produced larger artifact. Overall, in ultrasound imaging higher density of the material and rougher surface forces the creation of larger artifact.

Table 16. Artifact affected area in US with 7.5 MHz and 6.5 Mhz probes

US	7.5 MHz probe	6.5 MHz probe
Sample	Artifact affected area, mm ²	
Zr	22659	643
Stainless steel	70550	23549
K	7512	14873
E-max	26749	9487
Aluminium	34818	30121



Figure 9. US imaging of Zr sample in water with 7.5 MHz probe



Figure 10. US imaging of Zr sample in water with 6.5 MHz probe

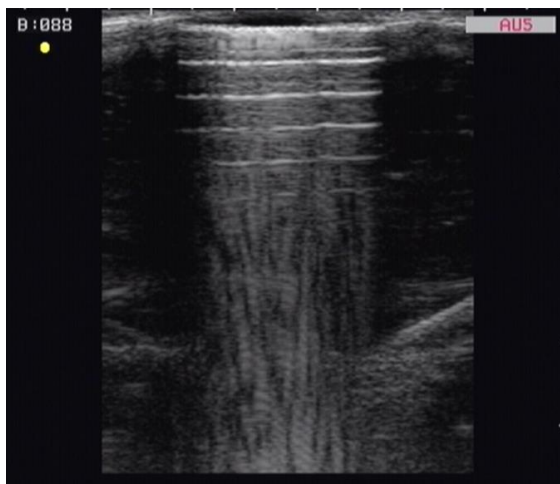


Figure 11. US imaging of Stainless steel (SS) sample in water with 7.5 MHz probe

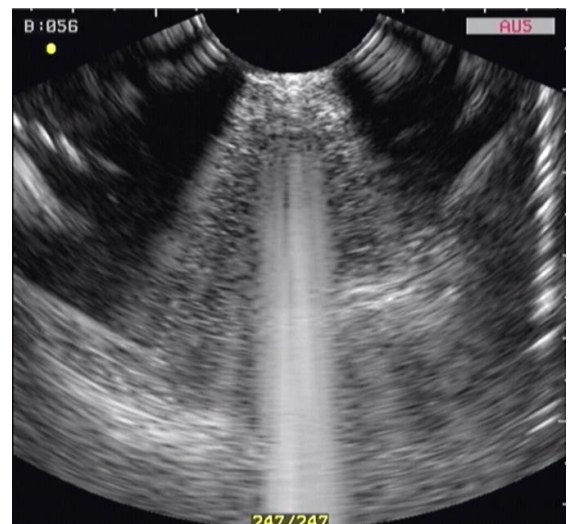


Figure 12. US imaging of Stainless steel (SS) sample in water with 6.5 MHz probe

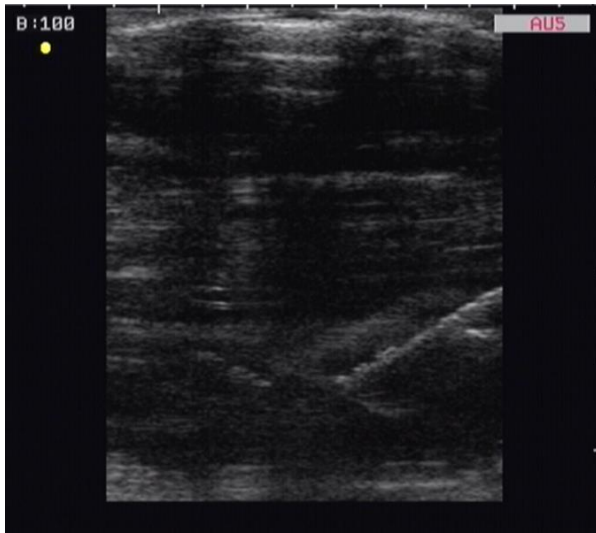


Figure 13. US imaging of **K** sample in water with 7.5 MHz probe



Figure 14. US imaging of **K** sample in water with 6.5 MHz probe

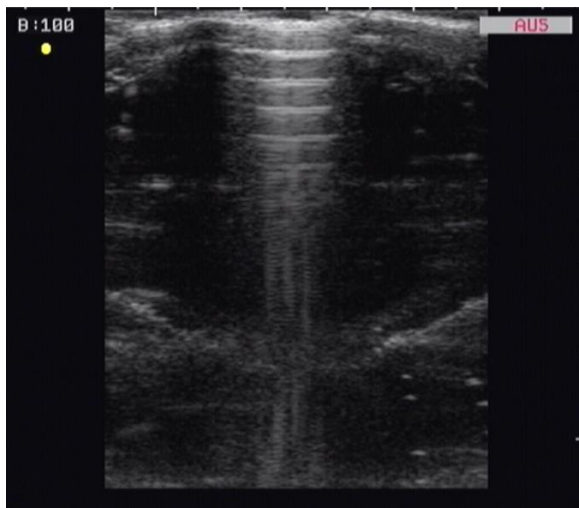


Figure 15. US imaging of **E-max** sample in water with 7.5 MHz probe



Figure 16. US imaging of **E-max** sample in water with 6.5 MHz probe

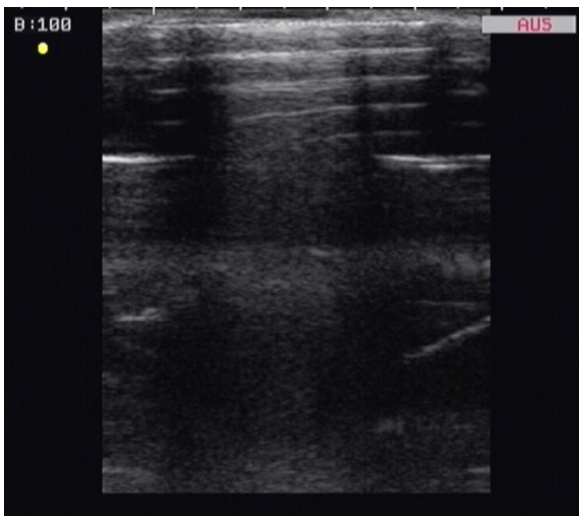


Figure 17. US imaging of Aluminium (**Al**) sample in water with 7.5 MHz probe



Figure 18. US imaging of Aluminium (**Al**) sample in water with 6.5 MHz probe

After performing the 2D overlay of artifacts for each sample, it is clearly visible, that Zr sample (Figure 19) produced the largest artifact in CBCT kV imaging with water and the smallest artifact in MR imaging. Stainless steel sample (Figure 20) created the greatest artifact and distortion in MR imaging, following up with CBCT kV imaging with water, but exhibited the least artifact in CBCT MV imaging without water. K sample (Figure 21) managed to create a significant artifact only in CBCT kV imaging with water, whereas in other combinations and modalities the artifact was negligible and should not present difficulties during imaging. Just like before mentioned samples, E-max sample (Figure 22) exhibited the largest artifact in CBCT kV imaging with water, but artifacts in other modalities were somewhat similar, but bigger than in K sample (Figure 21). Overall, aluminium sample (Figure 23) produced the least artifacts, with biggest artifact exerted in CBCT kV imaging with water and then following up in MR imaging, where other modalities shown small artifacts.

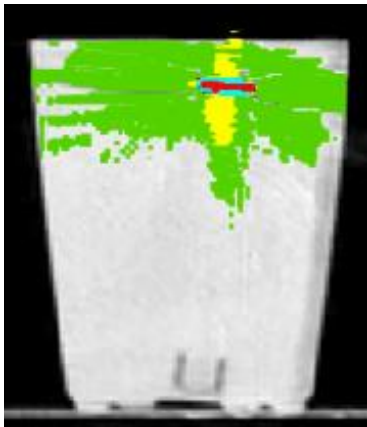


Figure 19. Overlay of all artifacts in a single slice **Zr** sample. CBCT kV with water (Green), CBCT kV without water (Blue), CBCT MV with water (Yellow), CBCT MV without water (Teal), MRI (Red).

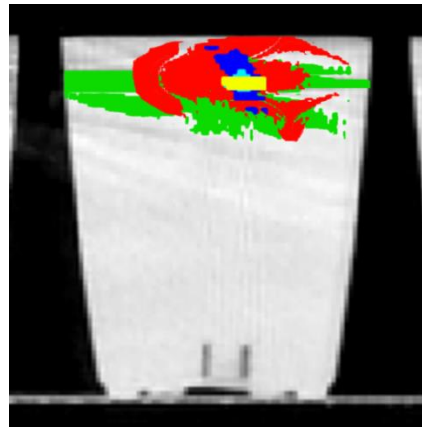


Figure 20. Overlay of all artifacts in a single slice **SS** sample. CBCT kV with water (Green), CBCT kV without water (Blue), CBCT MV with water (Yellow), CBCT MV without water (Teal), MRI (Red).

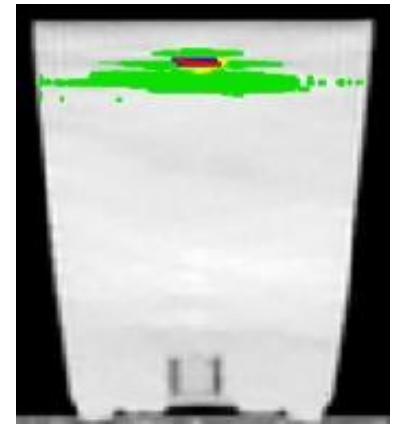


Figure 21. Overlay of all artifacts in a single slice **K** sample. CBCT kV with water (Green), CBCT kV without water (Blue), CBCT MV with water (Yellow), CBCT MV without water (Teal), MRI (Red).

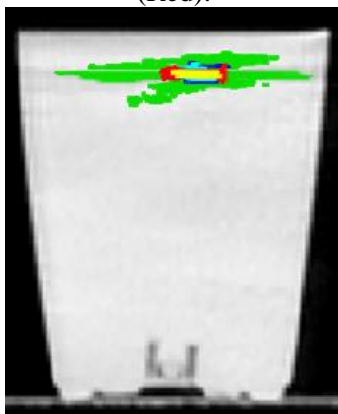


Figure 22. Overlay of all artifacts in a single slice **E-max** sample. CBCT kV with water (Green), CBCT kV without water (Blue), CBCT MV with water (Yellow), CBCT MV without water (Teal), MRI (Red).

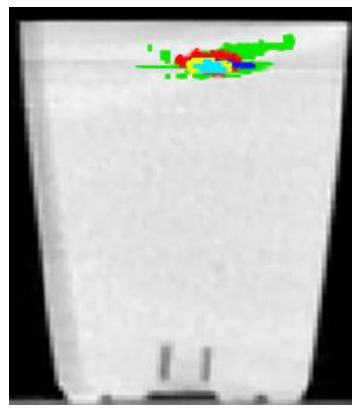


Figure 23. Overlay of all artifacts in a single slice **Al** sample. CBCT kV with water (Green), CBCT kV without water (Blue), CBCT MV with water (Yellow), CBCT MV without water (Teal), MRI (Red).

3.3. CNR calculation results

Contrast to noise ratio (CNR) determines the image quality. Usually the higher the CNR value, the easier it is to differentiate between the object and the background.

Table 17. CNR results after measuring and comparing unaffected and affected images in MRI

MRI	Unaffected image		Affected image		CNR (a/u)
Sample	Mean	Standard deviation	Mean	Standard deviation	
Zr	556.324	19.181	540.358	23.896	-0.73688
Stainless steel	504.466	30.549	90.253	61.152	-8.56939
K	556.747	29.477	516.278	36.255	-1.22484
E-max	561.352	19.711	526.577	47.093	-0.96332
Aluminium	553.059	32.599	473.028	107.357	-1.00877

For MRI CNR values should be positive if we would like to correctly visualise and differentiate tissues from the artifact. Stainless steel sample has produced the lowest CNR values (-8.56939 a/u), which are nearly 8 times lower than other samples (CNR values varying from -0.73688 a/u to -1.22484 a/u), therefore it means that noise in the image is higher than the contrast. According to table 17, K and aluminium samples provided CNR values of slightly above -1, of -1.22484 a/u and -1.00877 a/u, respectively. E-max and Zr samples produced the CNR values of -0.96332 a/u and -0.73688 a/u, respectively, which means that the Zr sample has distorted the MRI image the least and the image quality is the highest out of all samples. In this case, the CNR values in MR imaging are negative, therefore it would prove to be a challenge to properly differentiate between the tissue and the implant as the borders between them would be blurry and distorted.

Table 18. CNR results after measuring and comparing unaffected and affected images in CBCT kV with water

CBCT kV with H ₂ O	Unaffected image		Affected image		CNR (a/u)
Sample	Mean	Standard deviation	Mean	Standard deviation	
Zr	7.397	11.13	1588.983	2570.023	0.870295
Stainless steel	9.818	9.747	814.884	1897.065	0.600148
K	51.256	8.983	237.86	482.197	0.547187
E-max	34.05	7.518	200.818	534.748	0.440997
Aluminium	10.959	11.929	70.86	215.913	0.39175

In CBCT kV imaging with water CNR values have shown, that Zr sample (0.870295 a/u) should have had the highest image quality when comparing the object to the background, but the artifacted volume of said sample was the biggest one (16720.87 mm³). Therefore, CNR measurements for CBCT kV imaging with water should be interpreted in reverse, as lower CNR values mean that the artifacted volume was less, thus increasing the image quality. Stainless steel showed CNR value of 0.600148 a/u with an artifacting volume of 12540.62 mm³. It was observed that the K sample had a CNR value of 0.54718 a/u and artifacting volume of 6855.21 mm³. E-max and aluminium samples

had CNR values and artifacting volume of 0.440997 a/u and 8527.29 mm³, and 0.39175 a/u and 3344.54 mm³, respectively.

Table 19. CNR results after measuring and comparing unaffected and affected images in CBCT kV without water

CBCT kV without H ₂ O	Unaffected image		Affected image		CNR (a/u)
	Sample	Mean	Standard deviation	Mean	
Zr	-1000	0	143.488	2468.175	0.655195
Stainless steel	-1000	0	-439.653	1778.383	0.445602
K	-1000	0	-665.562	929.914	0.508613
E-max	-1000	0	-554.843	1152.424	0.546281
Aluminium	-1000	0	-846.339	505.834	0.429606

Results obtained in table 19 show that the CNR values of samples in CBCT kV imaging without water were somewhat similar, as values varied from 0.429606 a/u to 0.655195 a/u. With highest CNR values observed in Zr sample of 0.655195 a/u and lowest in aluminium sample with a value of 0.429606 a/u. CNR values of 0.445602 a/u, 0.508613 a/u and 0.546281 a/u were assigned to stainless steel, K and E-max samples, respectively.

Table 20. CNR results after measuring and comparing unaffected and affected images in CBCT MV with water

CBCT MV with H ₂ O	Unaffected image		Affected image		CNR (a/u)
	Sample	Mean	Standard deviation	Mean	
Zr	3.18	13.626	428.55	1075.056	0.55952
Stainless steel	3.55	36.372	277.66	701.788	0.551635
K	1.76	44.731	41.8	87.075	0.578442
E-max	13.26	59.268	117.98	242.53	0.593176
Aluminium	0.67	11.52	54.33	146.838	0.515222

Table 20 for CBCT MV imaging with water has shown that the CNR values of samples is similar, as the variation between values is less than 0.1 a/u and the artifacting volume of each sample is directly proportional to their CNR. Highest CNR was observed in E-max sample of 0.593176 a/u and an artifacting volume of 889.447 mm³ and the lowest was seen in aluminium (CNR 0.515222 a/u; artifacting volume 1994.31 mm³). Zr and stainless steel CNR was very similar, but artifacting volumes differing 300 mm³ as the values were 0.55952 a/u and 1727.94 mm³, and 0.551635 a/u and 1478.58 mm³ respectively, with K sample showing 0.578442 a/u and artifacting volume of 896.396 mm³.

Results obtained in table 21 show that the CNR values of samples in CBCT MV imaging without water were in a range between 0.647331 a/u and 0.757356 a/u. With highest CNR values observed in E-max sample of 0.757356 a/u and lowest in stainless steel sample with a value of 0.647331 a/u. Zr, K and aluminium samples had shown values of 0.668243 a/u, 0.681485 a/u and 0.651022 a/u, respectively.

Table 21. CNR results after measuring and comparing unaffected and affected images in CBCT MV without water

CBCT MV without H ₂ O	Unaffected image		Affected image		CNR (a/u)
	Mean	Standard deviation	Mean	Standard deviation	
Zr	-1000	0	-307.08	1466.438	0.668243
Stainless steel	-1000	0	-566.52	947.017	0.647331
K	-1000	0	-871.89	265.853	0.681485
E-max	-1000	0	-761.71	444.96	0.757356
Aluminium	-1000	0	-884.45	251.009	0.651022

CNR in performed CT imaging variations have resulted in a positive value, which leads to the fact that the image quality is reduced due to obstructive artifacting and additional noise. Therefore, in this case CBCT kV imaging with water show that CNR values are proportional to artifacting volume, but in reverse order. In CBCT MV imaging with water it was noted that CNR values are proportional to artifacting volumes of the samples in correct order, where higher CNR value meant, that the artifacted volume was the lowest. CNR values from CBCT imaging without water in kV and MV seem to be incoherent when compared to the artifact volume produced.

Overall, artifacts are created differently in MRI, CT and US modalities depending on the physics behind them. But the knowledge of properties of the materials imaged in these modalities assists in differentiation on which modality is best to use in certain situations, whether a person has ceramic type implants or metal based stainless steel or aluminium implants. Electroconductive, ferromagnetic and poor heat conductivity materials are not suited for MR imaging, as can be seen with the imaging results of stainless steel sample. If the implant material has high density values and X-ray attenuation coefficient, then the medical implant is not suited for CT imaging and would be imaged better in a MRI machine. Materials with high density and rough surface will produce the highest amount of reverberation artifact in any US imaging modality as sound reverberates stronger in high density materials. On the other hand, the artifacts can be reduced in all modalities with usage of various imaging techniques and artificial intelligence. In MR imaging, the artifact reduction is achieved by using VAT, MAVRIC and SEMAC algorithms at the cost of increased scanning times and heat absorbed by the medical implant. Artifact reduction in CT imaging can be obtained with the usage of combination between generative adversarial networks and metal artifact reduction algorithms, as this combination produces and compares the original image whilst transformed into a sinogram with the corrected sinogram and then combines both sinograms to create an image with fewer artifacts. For artifact reduction in US imaging, morphological image processing is used, which alters pixels of the image, but require extensive knowledge of denoising filters and external software and hardware. The developed measurement method for artifact evaluation was successful, as 3D modelled sample holder proved to not create any additional artifacts while being imaged with artifact exhibiting materials. Volume calculations were performed consistently, with 3D Slicer application and pixel value thresholding, 2D image analysis of US images and contrast to noise ratio for determination of image quality was successfully achieved by Image J software and shown valuable results, which can be used in further researches.

Conclusions

1. Artifacts are created differently in MRI, CT and US modalities depending on the physics behind them. Different material properties will affect different imaging modalities according their physical properties, including surface roughness, magnetic permeability, dielectric constant, physical density, effective Z number. Efficient artifact reduction methods exist and are proven, but in most cases increases the diagnostic procedure duration/reduces resolution of the image/are not fully effective.
2. Extensive literature analysis has shown that the most common materials in head and neck region are orthodontic appliances, which consist of dental implant itself, dental filling, brackets or screws. Stainless steel (DIN 316L), aluminium, dental implant material of Zr series Katana Zirconia STML. Dental filling of K series ENAMEL plus HRi biofunction (MICERIUM S.p.A, Italy). Dental implant material of E-max series Ivoclar Vivadent IPS E.max press, are the most popular materials for head and neck region medical implants.
3. Artifacting evaluation method was successfully developed by the use of open-source software tools. 3DSlicer programme was used to reconstruct 3D models of the artefact volumes for multislice evaluation. ImageJ was used for image thresholding, segmentation, contouring and final registration between modalities as one of the main measures of image quality - contrast-to-noise ratio was selected.
4. Evaluation with select materials lead to a conclusion, that artifact volume was observed in CBCT kV imaging with water, with values ranging from 3344.54 mm³ to 16720.87 mm³, and the smallest artifact volume was detected in CBCT MV imaging without water, with ranges from 301.115 mm³ to 1074.75 mm³. Stainless steel sample has proved to be the most artifacting medical material, with volume values ranging from 1074.75 mm³ to 25493.33 mm³ across modalities, whereas K sample has shown the least amount of artifacting, with values from 266.79 mm³ to 6855.21 mm³ across imaging modalities.

List of references

1. BOUSERHAL C, JACOBS R, QUIRYNEN M, VAN STEENBERGHE D. Imaging technique selection for the preoperative planning of oral implants: a review of the literature. *Clin Implant Dent Relat Res.* 2002;4(3):156-72. doi: 10.1111/j.1708-8208.2002.tb00167.x. PMID: 12516649.
2. ALLEN F, SMITH DG. An assessment of the accuracy of ridge-mapping in planning implant therapy for the anterior maxilla. *Clin Oral Implants Res.* 2000 Feb;11(1):34-8. doi: 10.1034/j.1600-0501.2000.011001034.x. PMID: 11168191.
3. KLINKE T, DABOUL A, MARON J, et al. Artifacts in magnetic resonance imaging and computed tomography caused by dental materials. *PLoS One.* 2012;7(2):e31766. doi:10.1371/journal.pone.0031766
4. BEUF O, LISSAC M, CRÉMILLIEUX Y, BRIGUET A. Correlation between magnetic resonance imaging disturbances and the magnetic susceptibility of dental materials. *Dent Mater.* 1994 Jul;10(4):265-8. doi: 10.1016/0109-5641(94)90072-8. PMID: 7664995.
5. ABBASZADEH K, HEFFEZ LB, MAFEE MF. Effect of interference of metallic objects on interpretation of T1-weighted magnetic resonance images in the maxillofacial region. *Oral Surg Oral Med Oral Pathol Oral Radiol Endod.* 2000 Jun;89(6):759-65. doi: 10.1067/moe.2000.105942. PMID: 10846134.
6. ANAN NUGROHO, RISANURI HIDAYAT, and HANUNG ADI NUGROHO. 2019. Artifact removal in radiological ultrasound images using selective and adaptive median filter. In *Proceedings of the 3rd International Conference on Cryptography, Security and Privacy (ICCSPP '19)*. Association for Computing Machinery, New York, NY, USA, 237–241. <https://doi.org/10.1145/3309074.3309119>
7. ELANGO VAN, A., & JEYASEELAN, T. Medical imaging modalities: A survey. 2016 *International Conference on Emerging Trends in Engineering, Technology and Science (ICETETS)*, 2016, 1-4.
8. MANSFIELD, P et al. “Active acoustic screening: reduction of noise in gradient coils by Lorentz force balancing.” *Magnetic resonance in medicine* vol. 33,2 (1995): 276-81. doi:10.1002/mrm.1910330220
9. POOLEY, R. A. *Fundamental Physics of MR Imaging.* RadioGraphics, 2005, 25(4), 1087–1099. doi:10.1148/rg.254055027
10. STANKOVIC JB, MILOSEVIC NT. *Osnovi radioloske fizike (Basic Principles of Radiological Physics)*, PTT, Belgrade, 2007
11. THOMAS AMK, BANERJEE AK, BUSCH U. *Classic Papers in Modern Diagnostic Radiology.* (2004) ISBN: 9783540219279
12. BUSHBERG JT, SEIBERT JA, JR. EML et-al. *The Essential Physics of Medical Imaging* (2011). LWW. ISBN:0781780578
13. VICTOR F. HUMPHREY, *Ultrasound and matter—Physical interactions*, *Progress in Biophysics and Molecular Biology*, Volume 93, Issues 1–3, 2007, Pages 195-211, ISSN 0079-6107, <https://doi.org/10.1016/j.pbiomolbio.2006.07.024>.

14. FELDMAN, MYRA K et al. "US artifacts." *Radiographics : a review publication of the Radiological Society of North America, Inc* vol. 29,4 (2009): 1179-89. doi:10.1148/rg.294085199
15. ALLISY-ROBERTS, P., WILLIAMS, J. R., & FARR, R. F. (2008). *Farr's physics for medical imaging*. Edinburgh: Saunders.
16. AVRUCH, L, AND P L COOPERBERG. "The ring-down artifact." *Journal of ultrasound in medicine : official journal of the American Institute of Ultrasound in Medicine* vol. 4,1 (1985): 21-8. doi:10.7863/jum.1985.4.1.21
17. TCHELEPI, HISHAM, and PHILIP W RALLS. "Color comet-tail artifact: clinical applications." *AJR. American journal of roentgenology* vol. 192,1 (2009): 11-8. doi:10.2214/AJR.07.3893
18. ALEXIS R. BOSCAK, MAHMOUD AL-HAWARY, and STEPHEN R. RAMSBURGH, Adenomyomatosis of the Gallbladder, *RadioGraphics* 2006 26:3, 941-946
19. CHAN, VINCENT & PERLAS, ANAHI. *Basics of Ultrasound Imaging* (2011) 10.1007/978-1-4419-1681-5_2.
20. MICHAEL BAAD, ZHENG FENG LU, INGRID REISER, and DAVID PAUSHTER, Clinical Significance of US Artifacts, *RadioGraphics* 2017 37:5, 1408-1423
21. LIN, EDWARD P et al. "Diagnostic clues to ectopic pregnancy." *Radiographics : a review publication of the Radiological Society of North America, Inc* vol. 28,6 (2008): 1661-71. doi:10.1148/rg.286085506
22. LEVINE, DEBORAH. "Ectopic pregnancy." *Radiology* vol. 245,2 (2007): 385-97. doi:10.1148/radiol.2452061031
23. ABU-ZIDAN, FIKRI M et al. "Clinical ultrasound physics." *Journal of emergencies, trauma, and shock* vol. 4,4 (2011): 501-3. doi:10.4103/0974-2700.86646
24. TRICHE, BENJAMIN L et al. "Recognizing and Minimizing Artifacts at CT, MRI, US, and Molecular Imaging." *Radiographics : a review publication of the Radiological Society of North America, Inc* vol. 39,4 (2019): 1017-1018. doi:10.1148/rg.2019180022
25. PENELOPE ALLISY-ROBERTS, JERRY R. WILLIAMS. *Farr's Physics for Medical Imaging*. (2021) ISBN: 9780702028441
26. JULIA F. BARRETT and NICHOLAS KEAT, *Artifacts in CT: Recognition and Avoidance*, *RadioGraphics* 2004 24:6, 1679-1691
27. CHAVHAN GB. *MRI Made Easy*. Jaypee Brothers Medical Publishers. (2013) ISBN:9350902702
28. Jackson, J et al. "Low-frequency restoration." *Magnetic resonance in medicine* vol. 11,2 (1989): 248-57. doi:10.1002/mrm.1910110213
29. YANASAK, NATHAN E, AND MICHAEL J KELLY. "MR imaging artifacts and parallel imaging techniques with calibration scanning: a new twist on old problems." *Radiographics : a review publication of the Radiological Society of North America, Inc* vol. 34,2 (2014): 532-48. doi:10.1148/rg.342135051

30. SCHICK, FRITZ. "Whole-body MRI at high field: technical limits and clinical potential." *European radiology* vol. 15,5 (2005): 946-59. doi:10.1007/s00330-005-2678-0
31. SMITH, R C et al. "Chemical shift artifact: dependence on shape and orientation of the lipid-water interface." *Radiology* vol. 181,1 (1991): 225-9. doi:10.1148/radiology.181.1.1887036
32. GOLD, GARRY E et al. "Musculoskeletal MRI at 3.0 T: initial clinical experience." *AJR. American journal of roentgenology* vol. 183,5 (2004): 1479-86. doi:10.2214/ajr.183.5.1831479
33. BALLINGER, J., MURPHY, A. Zero fill artifact. Reference article, Radiopaedia.org. (2013) <https://doi.org/10.53347/rID-22025>
34. DZMITRY M. FURSEVICH, GARY M. LIMARZI, MATTHEW C. O'DELL, MANUEL A. HERNANDEZ, and WILLIAM F. SENSACOVIC, *Bariatric CT Imaging: Challenges and Solutions*, *RadioGraphics* 2016 36:4, 1076-1086
35. PATEL, PRITESH & SEETHAMRAJU, RAVI & KIRSCH, JOHN & HAHN, PETER & GUIMARAES, ALEXANDER. *Body MR Imaging: Artifacts, k-Space, and Solutions*. *Radiographics : a review publication of the Radiological Society of North America, Inc.* 2013, 35. 10.1148/rg.2015140289.
36. KNOTT, P. T., MARDJETKO, S. M., KIM, R. H., COTTER, T. M., DUNN, M. M., PATEL, S. T., et. al. A comparison of magnetic and radiographic imaging artifact after using three types of metal rods: stainless steel, titanium, and vitallium. *The Spine Journal*, 2010 10(9), 789–794. doi:10.1016/j.spinee.2010.06.006
37. PROBST, FA, SCHWEIGER, J, STUMBAUM, MJ, KARAMPINOS, D, BURIAN, E, PROBST, M. Magnetic resonance imaging based computer-guided dental implant surgery—A clinical pilot study. *Clin Implant Dent Relat Res.* 2020; 22: 612–621. <https://doi.org/10.1111/cid.12939>
38. NIRAJ, L. K., PATTHI, B., SINGLA, A., GUPTA, R., ALI, I., DHAMA, K., KUMAR, J. K., & PRASAD, M. MRI in Dentistry- A Future Towards Radiation Free Imaging - Systematic Review. *Journal of clinical and diagnostic research : JCDR*, 2016 10(10), ZE14–ZE19. <https://doi.org/10.7860/JCDR/2016/19435.8658>
39. TYMOFIYEVA, O., VAEGLER, S., ROTTNER, K., BOLDT, J., HOPFGARTNER, A. J., PROFF, P. C., RICHTER, E. J., & JAKOB, P. M. Influence of dental materials on dental MRI. *Dento maxillo facial radiology*, 2013 42(6), 20120271. <https://doi.org/10.1259/dmfr.20120271>
40. GOWDA, E. & SAHOO, N.K. MRI Compatibility of Dental Materials. Volume – 3, Issue – 4, July - August - 2020, Page No. : 19 – 24 Access: [https://www.researchgate.net/publication/343975783 MRI Compatibility of Dental Materials](https://www.researchgate.net/publication/343975783_MRI_Compatibility_of_Dental_Materials)
41. HAYASHI, N., OGURA, A., TSUCHIHASHI, T. et al. Magnetization and demagnetization of magnetic dental attachments in a 3-T MRI system. *Radiol Phys Technol* 10, 294–300 (2017). <https://doi.org/10.1007/s12194-017-0399-0>
42. CHOCKATTU, S. J., SURYAKANT, D. B., & THAKUR, S. Unwanted effects due to interactions between dental materials and magnetic resonance imaging: a review of the

literature. *Restorative dentistry & endodontics*, 2018 43(4), e39.
<https://doi.org/10.5395/rde.2018.43.e39>

43. STARCUKOVÁ J, STARCUK Z JR, HUBÁLKOVÁ H, LINETSKIY I. Magnetic susceptibility and electrical conductivity of metallic dental materials and their impact on MR imaging artifacts. *Dent Mater*. 2008 Jun;24(6):715-23. doi: 10.1016/j.dental.2007.07.002. Epub 2007 Sep 19. PMID: 17884157.
44. JOHN N. MORELLI, VAL M. RUNGE, FEI AI, ULRIKE ATTENBERGER, LAN VU, STUART H. SCHMEETS, WOLFGANG R. NITZ, and JOHN E. KIRSCH. An Image-based Approach to Understanding the Physics of MR Artifacts *RadioGraphics* 2011 31:3, 849-866. Access: <https://pubs.rsna.org/doi/10.1148/rg.313105115>
45. BRETT S. TALBOT and ERIC P. WEINBERG. MR Imaging with Metal-suppression Sequences for Evaluation of Total Joint Arthroplasty. *RadioGraphics* 2016 36:1, 209-225. Access: <https://pubs.rsna.org/doi/10.1148/rg.2016150075>
46. BUTTS K, PAULY JM, GOLD GE. Reduction of blurring in view angle tilting MRI. *Magn Reson Med*. 2005 Feb;53(2):418-24. doi: 10.1002/mrm.20375. PMID: 15678535.
47. KOCH KM, LORBIECKI JE, HINKS RS, KING KF. A multispectral three-dimensional acquisition technique for imaging near metal implants. *Magn Reson Med*. 2009 Feb;61(2):381-90. doi: 10.1002/mrm.21856. PMID: 19165901.
48. LUKAS FILLI, MD,* LUKAS JUD, MD,* ROGER LUECHINGER, PHD,† DANIEL NANZ, PHD,* GUSTAV ANDREISEK, MD, MBA, VAL M. RUNGE, MD, SEBASTIAN KOZERKE, PHD,† AND NADJA A. FARSHAD-AMACKER, MD* Material-Dependent Implant Artifact Reduction Using SEMAC-VAT and MAVRIC. A Prospective MRI Phantom Study. 2017;52: 381-387. Access: <https://boris.unibe.ch/107765/1/00004424-201706000-00009.pdf>
49. SMITH, M. R., ARTZ, N. S., WIENS, C., HERNANDO, D., & REEDER, S. B. Characterizing the limits of MRI near metallic prostheses. *Magnetic resonance in medicine*, 2015 74(6), 1564–1573. Access: <https://doi.org/10.1002/mrm.25540>
50. LU, W., PAULY, K. B., GOLD, G. E., PAULY, J. M., & HARGREAVES, B. A. SEMAC: Slice Encoding for Metal Artifact Correction in MRI. *Magnetic resonance in medicine*, 2009, 62(1), 66–76. <https://doi.org/10.1002/mrm.21967>
51. WELLENBERG, R. H. H., HAKVOORT, E. T., SLUMP, C. H., BOOMSMA, M. F., MAAS, M., & STREEKSTRA, G. J. Metal artifact reduction techniques in musculoskeletal CT-imaging. *European Journal of Radiology*, 2018, 107, 60–69. doi:10.1016/j.ejrad.2018.08.010
52. W.A. KALENDER, R. HEBEL, J. EBERSBERGER, Reduction of CT artifacts caused by metallic implants., *Radiology*. 164 (1987) 576–577. doi:10.1148/radiology.164.2.3602406.
53. M.M. LELL, J.E. WILDBERGER, H. ALKADHI, J. DAMILAKIS, M. KACHELRIESS, Evolution in Computed Tomography: The Battle for Speed and Dose., *Invest. Radiol*. 50 (2015) 629–44. doi:10.1097/RLI.0000000000000172.
54. Y. CHEN, Y. LI, H. GUO, Y. HU, L. LUO, X. YIN, et al., CT metal artifact reduction method based on improved image segmentation and sinogram in-painting, *Math. Probl. Eng*. 2012 (2012) 1–19. doi:10.1155/2012/786281.

55. <https://www.gehealthcare.com/products/computed-tomography/radiation-therapy-planning/metal-artifact-reduction#:~:text=MAR%20is%20designed%20to%20reveal,contour%20targets%20with%20greater%20confidence.>
56. YOU C, LI G, ZHANG Y, ZHANG X, SHAN H, LI M, JU S, ZHAO Z, ZHANG Z, CONG W, VANNIER MW, SAHA PK, HOFFMAN EA, WANG G. CT Super-Resolution GAN Constrained by the Identical, Residual, and Cycle Learning Ensemble (GAN-CIRCLE). *IEEE Trans Med Imaging*. 2020 Jan;39(1):188-203. doi: 10.1109/TMI.2019.2922960. Epub 2019 Jun 14. PMID: 31217097.
57. SHIN Y, YANG J, LEE YH. Deep Generative Adversarial Networks: Applications in Musculoskeletal Imaging. *Radiol Artif Intell*. 2021;3(3):e200157. Published 2021 Mar 3. doi:10.1148/ryai.2021200157
58. YI, X., WALIA, E., & BABYN, P. Generative Adversarial Network in Medical Imaging: A Review. *Medical Image Analysis*, 2019, 101552. doi:10.1016/j.media.2019.101552
59. KOIKE Y, ANETAI Y, TAKEGAWA H, et al. Deep learning-based metal artifact reduction using cycle-consistent adversarial network for intensity-modulated head and neck radiation therapy treatment planning. *Phys Med*. 2020;78:8–14. <https://doi.org/10.1016/j.ejmp.2020.08.018>
60. T.R.C. JOHNSON, Dual-energy CT: general principles., *AJR. Am. J. Roentgenol*. 199 (2012) 3–8. doi:10.2214/AJR.12.9116
61. P. KOMLOSI, D. GRADY, J.S. SMITH, C.I. SHAFFREY, A.R. GOODE, P.G. JUDY, et al., Evaluation of monoenergetic imaging to reduce metallic instrumentation artifacts in computed tomography of the cervical spine, *J Neurosurg Spine*. 22 (2015) 34–38. doi:10.3171/2014.10.SPINE14463
62. K.L. GRANT, T.G. FLOHR, B. KRAUSS, M. SEDLMAIR, C. THOMAS, B. SCHMIDT, Assessment of an Advanced Image-Based Technique to Calculate Virtual Monoenergetic Computed Tomographic Images From a Dual-Energy Examination to Improve Contrast-To-Noise Ratio in Examinations Using Iodinated Contrast Media, *Invest. Radiol*. 49 (2014) 586–592. doi:10.1097/RLI.0000000000000060.
63. S. KUCHENBECKER, S. FABY, S. SAWALL, M. LELL, M. KACHELRIEß, Dual energy CT: how well can pseudo-monochromatic imaging reduce metal artifacts?, *Med. Phys*. 42 (2015) 1023–1036. doi:10.1118/1.4905106
64. FELDMAN, M. K., KATYAL, S., & BLACKWOOD, M. S. US Artifacts. *RadioGraphics*, 2009, 29(4), 1179–1189. doi:10.1148/rg.294085199
65. EP, S., & AL-SAQRI, K. S. M. Reduction of Ultrasound Imaging Artifacts. *Journal of Student Research*. 2017. <https://doi.org/10.47611/jsr.vi.550>
66. HUANG, C., SONG, P., TRZASKO, J. D., GONG, P., LOK, U.-W., TANG, S., CHEN, S. Simultaneous Noise Suppression and Incoherent Artifact Reduction in Ultrafast Ultrasound Vascular Imaging. *IEEE Transactions on Ultrasonics, Ferroelectrics, and Frequency Control*, 2021, 68(6), 2075–2085. doi:10.1109/tuffc.2021.3055498

67. S. SUDHA, G. SURESH AND R. SUKANESH, "Comparative Study on Speckle Noise Suppression Techniques for Ultrasound Images", *International Journal of Engineering and Technology*, vol. 1, no. 1, pp. 57-62, 2009
68. YAEL EREZ, YOAV Y. SCHECHNER, AND DAN ADAM, "Ultrasound image denoising by spatially varying frequency compounding", *Proc. DAGM Symposium, Lecture notes on computer science* Vol. 4147, pp. 1-10, 2006
69. HULBERT SF, BENNETT JT. State of the art in dental implants. *J Dent Res.* 1975 Jun;54 Spec No B:B153-7. doi: 10.1177/00220345750540021001. PMID: 1055740.
70. SYKARAS N, IACOPINO AM, MARKER VA, TRIPLETT RG, WOODY RD. Implant materials, designs, and surface topographies: their effect on osseointegration. A literature review. *Int J Oral Maxillofac Implants.* 2000 Sep-Oct;15(5):675-90. PMID: 11055135.
71. WENNERBERG A, ALBREKTSSON T. On implant surfaces: a review of current knowledge and opinions. *Int J Oral Maxillofac Implants.* 2010 Jan-Feb;25(1):63-74. PMID: 20209188.
72. CHATURVEDI TP. An overview of the corrosion aspect of dental implants (titanium and its alloys). *Indian J Dent Res.* 2009 Jan-Mar;20(1):91-8. doi: 10.4103/0970-9290.49068. PMID: 19336868.
73. SAINI, M., SINGH, Y., ARORA, P., ARORA, V., & JAIN, K. Implant biomaterials: A comprehensive review. *World journal of clinical cases*, 2015, 3(1), 52–57. <https://doi.org/10.12998/wjcc.v3.i1.52>
74. ADYA N, ALAM M, RAVINDRANATH T, MUBEEN A, SALUJA B. Corrosion in titanium dental implants: literature review. *Journal of Indian Prosthodontic Society.* 2005;5:126–131
75. W. NICHOLSON, J. Titanium Alloys for Dental Implants: A Review. *Prosthesis*, 2020, 2(2), 100–116. <https://doi.org/10.3390/prosthesis2020011>
76. LEE, E. H., BYUN, T. S., HUNN, J. D., YOO, M. H., FARRELL, K., & MANSUR, L. K. On the origin of deformation microstructures in austenitic stainless steel: part I—microstructures. *Acta Materialia*, 2001, 49(16), 3269–3276. doi:10.1016/s1359-6454(01)00193-8
77. DAI, Y., EGELAND, G. W., & LONG, B. Tensile properties of EC316LN irradiated in SINQ to 20dpa. *Journal of Nuclear Materials*, 2008, 377(1), 109–114. doi:10.1016/j.jnucmat.2008.02.035
78. LEE, D. J., BYUN, J. C., SUNG, J. H., & LEE, H. W. The dependence of crack properties on the Cr/Ni equivalent ratio in AISI 304L austenitic stainless steel weld metals. *Materials Science and Engineering: A*, 2009, 513-514, 154–159. doi:10.1016/j.msea.2009.01.049
79. GEANTA, VICTOR & VOICULESCU, IONELIA & ȘTEFĂNOIU, RADU & RUSU, ELENA. Stainless Steels with Biocompatible Properties for Medical Devices. *Key Engineering Materials*. 2013, 583. 9-15. 10.4028/www.scientific.net/KEM.583.9.
80. <https://www.materialwelding.com/wp-content/uploads/2022/02/schaeffler-diagram-1.jpg?ezimgfmt=ng:webp/ngcb4>
81. HAASE, FABIAN & SIEMERS, CARSTEN & KLINGE, LINA & LU, CHENG & LANG, PATRIC & LEDERER, STEPHAN & KÖNIG, TILL & RÖSLER, JOACHIM. Aluminum-

- and Vanadium-free Titanium Alloys for Medical Applications. MATEC Web of Conferences. 2020, 321. [10.1051/matecconf/202032105008](https://doi.org/10.1051/matecconf/202032105008).
82. SCHUPBACH, P., GLAUSER, R., & BAUER, S. Al₂O₃ Particles on Titanium Dental Implant Systems following Sandblasting and Acid-Etching Process. *International Journal of Biomaterials*, 2019, 1–11. doi:10.1155/2019/6318429
 83. ABD EL-GHANY, O. S., & SHERIEF, A. H. Zirconia based ceramics, some clinical and biological aspects: Review. *Future Dental Journal*, 2016, 2(2), 55–64. doi:10.1016/j.fdj.2016.10.002
 84. WARRETH, A., & ELKAREIMI, Y. All-ceramic restorations: A review of the literature. *The Saudi dental journal*, 2020, 32(8), 365–372. <https://doi.org/10.1016/j.sdentj.2020.05.004>
 85. SARIDAG S, TAK O, ALNIACIK G. Basic properties and types of zirconia: An overview. *World J Stomatol* 2013; 2(3): 40-47 [DOI: [10.5321/wjs.v2.i3.40](https://doi.org/10.5321/wjs.v2.i3.40)]
 86. ÖZKURT, Z., & KAZAZOĞLU, E. Zirconia Dental Implants: A Literature Review. *Journal of Oral Implantology*, 2011, 37(3), 367–376. doi:10.1563/aaid-joi-d-09-00079
 87. BROCHU JF, EL-MOWAFY O. Longevity and clinical performance of IPS-Empress ceramic restorations – a literature review: *J Can Dent Assoc*. 2002;68(4):233-237
 88. HO, GARY & MATINLINNA, JUKKA. Insights on Ceramics as Dental Materials. Part I: Ceramic Material Types in Dentistry. *Silicon*. 2011. [10.1007/s12633-011-9078-7](https://doi.org/10.1007/s12633-011-9078-7).
 89. RITZBERGER, C., APEL, E., HÖLAND, W., PESCHKE, A., & RHEINBERGER, V. M. Properties and Clinical Application of Three Types of Dental Glass-Ceramics and Ceramics for CAD-CAM Technologies. *Materials*, 3(6), 2010, 3700–3713. <https://doi.org/10.3390/ma3063700>
 90. PICHÉ PW, O'BRIEN WJ, GROH CL, BOENKE KM. Leucite content of selected dental porcelains. *J Biomed Mater Res*. 1994 May;28(5):603-9. doi: [10.1002/jbm.820280510](https://doi.org/10.1002/jbm.820280510). PMID: 8027100.
 91. SMEETS, R., SCHÖLLCHEN, M., GAUER, T., AARABI, G., ASSAF, A. T., RENDENBACH, C., BECK-BROICHSITTER, B., SEMMUSCH, J., SEDLACIK, J., HEILAND, M., FIEHLER, J., & SIEMONSEN, S. Artefacts in multimodal imaging of titanium, zirconium and binary titanium-zirconium alloy dental implants: an in vitro study. *Dento maxillo facial radiology*, 2017, 46(2), 20160267. <https://doi.org/10.1259/dmfr.20160267>
 92. DUTTENHOEFER F, MERTENS M, VIZKELETY J, GREMSE F, STADELMANN V, SAUERBIER S. Magnetic resonance imaging in zirconia-based dental implantology. *Clin Oral Implants Res* 2015; 26: 1195–202. doi: <https://doi.org/10.1111/clr.12430>
 93. RAFAEL C. GONZALEZ, RICHARD E. WOODS, “Digital Image Processing,” Second Edition, Prentice Hall, p.519-560&617-621
 94. DILNA, K. & JUDE HEMANTH, D. Novel image enhancement approaches for despeckling in ultrasound images for fibroid detection in human uterus. *Open Computer Science*, 11(1), 2021, 399-410. <https://doi.org/10.1515/comp-2020-0140>

95. RODRÍGUEZ-MOLARES, ALFONSO & RINDAL, OLE MARIUS & D'HOOGHE, JAN & MÅSØY, SVEIN-ERIK & AUSTENG, ANDREAS & LEDIJU BELL, MUYINATU & TORP, HANS. The Generalized Contrast-to-Noise Ratio: A Formal Definition for Lesion Detectability. *IEEE Transactions on Ultrasonics, Ferroelectrics, and Frequency Control*. PP. 2019. 1-1. 10.1109/TUFFC.2019.2956855.
96. KAYACI, SELIM & TABAK, AHMET & DURUR-SUBASI, IRMAK & ELDEŞ, TUĞBA & KÖKSAL, VANER & SIRIN, MURAT & ARSLAN, YUSUF. Artifacts in cranial MRI caused by extracranial foreign bodies and analysis of these foreign bodies. *Indian Journal of Radiology and Imaging*. 2019. 29. 299. 10.4103/ijri.IJRI_211_18.
97. https://medical.fr/22582-medium_default/ge-mtz-65MHz-p9603au-curved-array-transducer-for-ge-logiq-200-series.jpg
98. https://www.minitube.com/userdata/dcshop/images/normal/23500-1107_Linear-probe.jpg
99. H. LEE, M.S. KIM, Y. PARK, An analytic network process approach to operationalization of five forces model, *Appl. Math. Model.* 36 (2012) 1783–1795, <https://doi.org/10.1016/j.apm.2011.09.012>
100. S. GUPTA, N.K. MALHOTRA, M.R. CZINKOTA, P. FOROUDI, Marketing innovation: a consequence of competitiveness, *J. Bus. Res.* 69 (12) (2016) 5671–5681, <https://doi.org/10.1016/j.jbusres.2016.02.042>